Characterization of an Integrating Sphere Setup for Measurements of Organic LEDs

Janne Askola

School of Electrical Engineering

Thesis submitted for examination for the degree of Master of Science in Technology.

Espoo 23.11.2015

Thesis supervisor:

Prof. Erkki Ikonen

Thesis advisors:

D.Sc. (Tech.) Tuomas Poikonen

M.Sc. (Tech.) Tomi Pulli

Aalto University
School of Electrical
Engineering

AALTO UNIVERSITY
SCHOOL OF ELECTRICAL ENGINEERING

ABSTRACT OF THE
MASTER'S THESIS

Author: Janne Askola

Title: Characterization of an Integrating Sphere Setup for Measurements of Organic LEDs

Date: 23.11.2015 Language: English Number of pages: 7+48

Department of Signal Processing and Acoustics

Professorship: Measurement Science and Technology

Supervisor: Prof. Erkki Ikonen

Advisors: D.Sc. (Tech.) Tuomas Poikonen, M.Sc. (Tech.) Tomi Pulli

Light emitting diodes have been replacing the conventional incandescent lamps in the recent years due to better energy efficiency. Organic LEDs are seen as one of the development directions for future lighting and their unique properties offer new luminaire design possibilities.

In this work, the measurement setup of luminous flux at Metrology Research Institute is optimized and characterized for OLED measurements. Improvements for measuring the spatial responsivity distribution function of the 1.65-m integrating sphere spectrally and photometrically with better signal-to-noise ratio were made. The spatial responsivity distribution function of the integrating sphere was scanned spectrally. Spatial correction coefficient was calculated for the tested OLEDs both photometrically and spectrally, finding out 0.5 % difference of the results.

The angular distribution of the tested OLEDs was measured in a goniospectrometer and it was found out that the OLEDs had different distributions based on their surface type. Edge emission of a tested OLED was 0.7 % of the main surface emission. The luminous flux of the OLEDs was measured in the integrating sphere setup and an expanded uncertainty ($k = 2$) of 0.88 % was determined for the luminous flux measurement of a typical OLED.

The work done in this thesis is part of the EMRP project ENG62 Metrology for Efficienct and Safe Innovative Lighting (MESaIL).

Keywords: OLED, Integrating Sphere, Photometry, Spatial correction, Luminous flux

AALTO-YLIOPISTO
SÄHKÖTEKNIIKAN KORKEAKOULU

DIPLOMITYÖN
TIIVISTELMÄ

Tekijä: Janne Askola

Työn nimi: Integroivan pallon karakterisointi orgaanisten LEDien mittauksiin

Päivämäärä: 23.11.2015 Kieli: Englanti Sivumäärä: 7+48

Signaalinkäsittelyn ja akustiikan laitos

Professuuri: Mittaustekniikka

Työn valvoja: Prof. Erkki Ikonen

Työn ohjaajat: TkT Tuomas Poikonen, DI Tomi Pulli

Hohtodiodit (LEDit) ovat viime vuosina korvanneet perinteisiä hehkulamppuja osaltaan paremman energiatehokkuuden vuoksi. Tulevaisuuden valaistuksen yksi kehityssuunta ovat orgaaniset LEDit (OLEDit). Niiden erikoislaatuiset ominaisuudet kuten esimerkiksi ohuus ja taipuisuus avaavat uusia mahdollisuuksia valaisinsuunnittelussa.

Tässä työssä optimoitiin ja karakterisoitiin MIKES-Aalto Mittaustekniikan valovirran mittausjärjestelmä OLEDien mittaamista varten. Integroivan pallon spatiaalivasteen spektristä ja fotometristä suuremmalla signaalikohinasuhteella mittaamista varten järjestelmää parannettiin ja integroivan pallon spatiaalivaste skannattiin spektrisesti. Spatiaalikorjauskertoimet laskettiin testatuille kuudelle OLEDille spektrisesti ja fotometrisesti, ja huomattiin 0,5 prosentin ero menetelmien välillä.

Testattujen OLEDien kulmavaste mitattiin goniospektrometrin avulla ja peili- ja mattapintaisten OLEDien vasteen huomattiin eroavan toisistaan. OLEDin reunasäteily mitattiin olevan 0,7 % kyseisen paneelin pääkeilan säteilystä. OLEDien valovirrat mitattiin integroivassa pallossa ja tyypillisen OLEDin laajennetuksi mittausepävarmuudeksi määritettiin 0.88 % ($k = 2$).

Tämä diplomityö tehtiin osana EMRP-projektia ENG62 Metrology for Efficienct and Safe Innovative Lighting (MESaIL).

Avainsanat: OLED, Integroiva pallo, Fotometria, Spatiaalikorjaus, Valovirta

Preface

The work leading to this thesis was carried out in Metrology Research Institute of Aalto University School of Electrical Engineering. The thesis was partly funded by The European Metrology Research Programme (EMRP) ENG62 Project Metrology for Efficient and Safe Innovative Lighting.

First I would like to thank Professor Erkki Ikonen for supervising this thesis and for the opportunity to work in the Metrology Research Institute. I am also grateful for my advisors D.Sc. (Tech.) Tuomas Poikonen and M.Sc. (Tech.) Tomi Pulli for their guidance throughout the thesis. It has been a pleasure to work with my colleagues at the Metrology Research Institute.

I would have not been able to reach this far without the help and support of my family, thank you! I am also deeply thankful for my friends who have stood by me through all my years of study.

And last, I want to thank the love of my life Hilla for being on my side through this journey.

Otaniemi, December 3rd 2015

Janne Askola

Contents

Symbols and abbreviations

Symbols

A_{ext}	area of the precision aperture
c	speed of light in vacuum $\approx 3 \times 10^8$ [m/s]
C	normalization constant
c_{e}	color correction for the external source
c_{i}	color correction for the internal source
$E(\lambda)$	spectral irradiance
E_{ext}	illuminance produced by the external source
E_{g}	energy gap between the HOMO and LUMO levels
$E_{\text{in}}(\lambda)$	spectrum of the tungsten reference lamp measured in the integrating sphere
$E_{\text{out}}(\lambda)$	spectrum of the tungsten reference lamp measured on optical rail
E_{v}	illuminance
f	combination of correction factors
$f(\theta_n)$	weighting factor of the spherical coordinate system
f_2	directional quality index
h	Planck constant
I	the signal from the detector
I_{rel}	relative intesity distribution of the light source
$K(\theta_n, \phi_m)$	spatial responsivity distribution function (SRDF)
$K^*(\theta_n, \phi_m)$	normalized spatial responsivity distribution function
$K^*_{\text{diff}}(\theta_n, \phi_m)$	relative difference of two SRDF
$K^*_{\text{RMS}}(\theta_n, \phi_m)$	weighted root-mean-square value of the relative difference of two SRDF
k_{a}	illuminance uniformity of the external source
k_{comp}	k_{int} for virtual ideal OLED
k_{ext}	spatial non-uniformity correction of the external source
k_{int}	spatial non-uniformity correction of the internal source
K_{m}	photopic normalization constant ≈ 683 [lm/W]
r	radius of a sphere
$R_{\text{D}}(\lambda)$	relative spectral responsivity of the detector
$R_{\text{S}}(\lambda)$	relative spectral responsivity of the integrating-sphere photometer
R_{v}	luminous responsivity of the detector
$S(\lambda)$	relative spectral output of the source
$S_{\text{A}}(\lambda)$	spectrum of the CIE Standard Illuminant A
$S_{\text{c}}(\lambda)$	relative spectral ouput of the calibration source
S_{DUT}	DUT signal of the self-absorption correction measurement
$S_{\text{e}}(\lambda)$	spectrum of the external source

S_{empty}	signal of the empty sphere in the self-absorption correction measurement
$S_{\text{i}}(\lambda)$	spectrum of the internal source
$T(\lambda)$	relative spectral throughput of the integrating sphere
$V(\lambda)$	relative spectral sensitivity of human eye
Y	signal produced by the internal source
Y_{ext}	signal produced by the external source
α	self-absorption correction coefficient
β	correction for the angle of incidence
λ	wavelength
Φ_{ext}	luminous flux of the external source
Φ_{v}	luminous flux
ρ	reflectance

Abbreviations

AEF	Aalto Energy Efficiency project
$BaSO_4$	Barium sulfate
CCT	correlated color temperature
CIE	Commission Internationale de l'Éclairage, International Commission on Illumination
DUT	device under test
E27	Edison light bulb screw, 27 mm diameter
EMRP	European Metrology Research Programme
HOMO	highest occupied molecular orbital
LED	light emitting diode
LUMO	lowest unoccupied molecular orbital
MESaIL	Metrology for Efficient and Safe Innovative Lighting, EMRP project
MRI	Metrology Research Institute
OLED	organic light emitting diode
RMS	root-mean-square
SNR	signal-to-noise ratio
SRDF	spatial responsivity distribution function
SSL	solid-state lighting

1 Introduction

In the recent years, inorganic light emitting diodes (LEDs) have been replacing the conventional incandescent lamps due to better energy efficiency. Solid-state lighting (SSL) is becoming more popular through the legislation and better availability of the products on the market. Organic LEDs (OLEDs) are one of the development directions for future lighting. They open up new luminaire design possibilities as compared to traditional lighting products due to their thin profile, large emitting area compared to traditional LEDs, and their unique properties, e.g. flexibility and translucency.

The luminous flux is the amount of total visible light weighted by the spectral responsivity of the human vision system produced by a light source and its unit is lumen. The problems of the SSL measurements have been studied in European Union projects Metrology for Solid State Lighting (Lighting, ENG05) and Metrology for Efficient and Safe Innovative Lighting (MESaIL, ENG62) and in Aalto Energy Efficiency (AEF) project funded by the Aalto University. This thesis is a part of the project MESaIL. [1, 2, 3]

The luminous flux of a light source is often measured using an integrating sphere. Ideally, the signal measured with an integrating sphere is directly proportional to the luminous flux of the light source inside the sphere. However, in reality, several correction factors based on, e.g., the intensity distribution and the spectrum of the source need to be applied to the results. Due to the non-isotropic radiation pattern of typical OLEDs and many other SSL products, the spatial non-uniformity correction can differ significantly from unity. In order to determine this correction, the angular distribution of the source needs to be measured and the spatial uniformity of the integrating sphere needs to be scanned accurately.

In this thesis, the integrating sphere based luminous flux setup of Metrology Research Institute is optimized and characterized for OLED measurements. For this purpose a new spectroradiometer diffuser head with a high throughput was developed and the output of the integrating sphere scanner is widened in the wavelength scale. The spatial uniformity of the integrating sphere was scanned spectrally using an array spectroradiometer as well as using a photometer. The spatial responsivity distribution maps were compared with each others photometrically and the responsivity of the sphere at different wavelengths was studied from the spectral map.

Furthermore, the goniometric setup introduced earlier in [4] is modified for OLED measurements. Both the main surface emission and the edge emission of the OLED is measured in the goniometer and the results are used for the spectral spatial correction in the integrating sphere measurements and to study the effect of the edge emission on the total luminous flux. The total luminous flux of the OLEDs are measured in the modified integrating sphere setup and the uncertainty budget for the OLED measurements in the characterized setup is given.

2 Technical background

The luminous flux of organic LEDs and other types of SSL products is measured at the Metrology Research Institute (MRI) using an integrating sphere setup. To understand the functionality of the integrating sphere and the measurement results, some background about photometry is needed. In this section, the operation principles of OLEDs are introduced and the basic details of photometry and the quantities used in this work are explained. The integrating sphere measurement setup is displayed with an explanation of the absolute integrating sphere method. The correction coefficients needed in the sphere measurements are explained. The goniospectrometer, that is utilized to determine the angular distribution of the measured lamp for calculating the spatial non-uniformity correction, and the different detectors operated in the measurements are introduced.

2.1 Organic light emitting diodes

Organic light emitting diodes (OLEDs) are thin, diffuse-area light sources with near-Lambertian emission characteristics. They are in their simplest form quite similar to the inorganic LEDs when the structure of the layers is observed. The structure of an OLED is shown in Figure 1. OLEDs have usually a metallic cathode and a transparent anode. In between the electrical contacts there is a thin organic layer, from 100 to 200 nm, in which the highest occupied molecular orbital (HOMO) and the lowest unoccupied molecular orbital (LUMO) act like the valence and the conduction bands in inorganic semiconductors. [5, 6, 7]

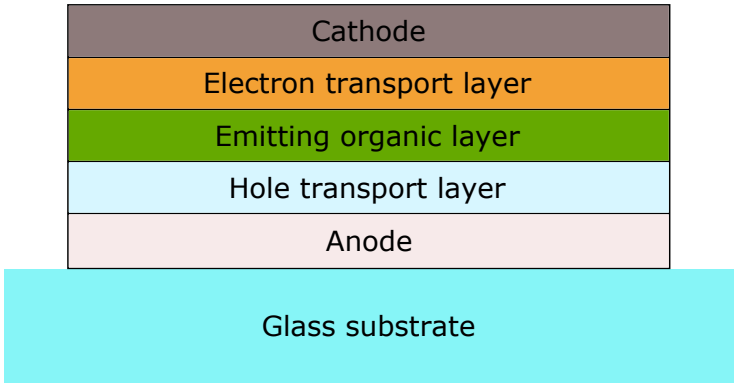

Figure 1: Basic physical structure of an OLED

In the electron-hole recombination between the HOMO and LUMO levels a photon, corresponding to the energy gap E_g between the levels, is emitted. The wavelength of the photon can be calculated by

$$\lambda = \frac{hc}{E_g}, \tag{1}$$

where h is the Planck constant and c is the speed of light in vacuum. An electron transport and a hole transport layers are needed to control the electron and hole

transportation from the cathode and the anode to the organic layer. This improves the efficiency of the device by helping more of the charge carriers to recombine. [8, 6]

The light emitted by the organic layer of an OLED is mostly out-coupled through the main surface of the panel. However, some of it is either trapped inside the panel for good or emitted through the edge of the glass substrate, based on the internal emission angle of the photon and the refractive indices of the materials. On the basis of previous studies, the light emitted by the edge of the OLED has similar angular distribution to the leaky waveguide modes. [9, 10]

White OLEDs can be achieved using many different methods that include having different emissive layers for different colors, using a phosphorescent layer to convert the energy of a blue emitter to longer wavelengths, creating a matrix of different color emitters, and different combinations of these techniques. In 2011 the state-of-the-art efficacy of a white OLED was 128 lm/W and a target for 2020 was set to 168 lm/W with 100 000 hour lifetime. [11]

With their thin profile, large emitting area, flexibility (Figure 2), OLEDs provide new possibilities for manufacturers of lighting products. At the moment OLEDs are used more as screens for hand-held devices and even for televisions than for illuminating purposes. [7, 11]

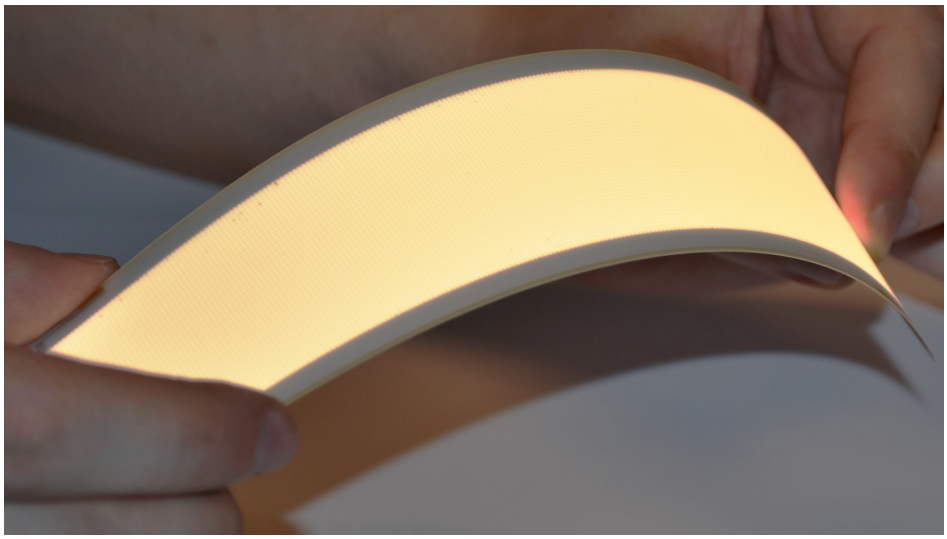

Figure 2: Flexible OLED in use

2.2 Principles of photometry

Human eye can detect electromagnetic radiation in the wavelength range of about 360–830 nm. The optical radiant energy of a light source can be measured radiometrically or photometrically. The photometric base quantity, luminous intensity (unit candela, cd), was historically defined with a flame of a candle. At present, candela is defined as *the luminous intensity, in a given direction, of a source that emits monochromatic radiation of frequency* 540×10^{12} *Hz and that has a radiant intensity in that direction of* $\frac{1}{683}$ *W/sr.* [12, 13]

Often the radiometric quantities are presented as a distribution with respect to the wavelength, e.g. spectral irradiance $E(\lambda)$. On the other hand, in photometry the quantities are weighted with the relative spectral sensitivity of the human eye $V(\lambda)$ (shown in Figure 3). The $V(\lambda)$ function, defined by the International Commission on Illumination (Commission Internationale de l'Éclairage, CIE), is non-zero at the wavelengths from 360 to 830 nm. The maximum value of the function is at 555 nm. Any photometric quantity X_v (v for visual) can be derived from the corresponding spectral radiometric quantity $X(\lambda)$ by

$$X_\mathrm{v} = K_\mathrm{m} \int_{360\ \mathrm{nm}}^{830\ \mathrm{nm}} X(\lambda) V(\lambda) \mathrm{d}\lambda, \tag{2}$$

where K_m (683 lm W^{-1}) is a normalization constant based on the definition of luminous intensity. [12, 14]

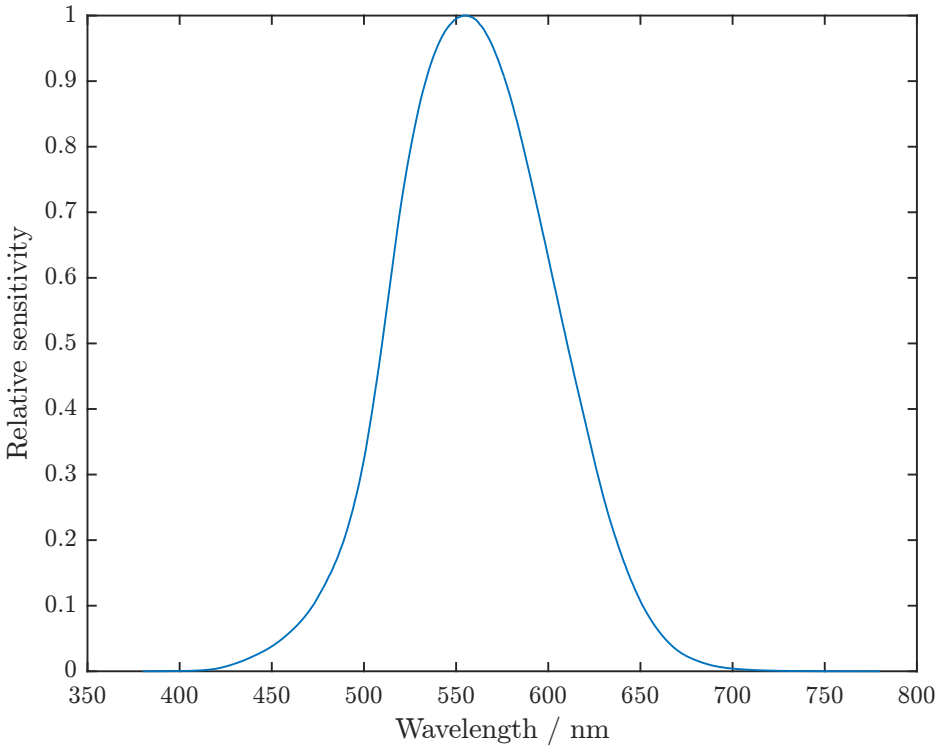

Figure 3: Relative photopic spectral sensitivity of the human eye, $V(\lambda)$.

A source with an isotropic luminous intensity of 1 cd has the luminous flux Φ_v of 1 lm over a solid angle of 1 sr. The illuminance E_v (unit lux, lx = $\mathrm{lm/m^2}$) is defined as the luminous flux that falls on to a surface.

Photometric quantities are typically measured with a photometer. It is a detector that is equipped with an optical filter to convert the normalized spectral response of the detector close to the $V(\lambda)$ function. The illuminance reaching the detector is calculated by

$$E_\mathrm{v} = \frac{I}{R_\mathrm{v}} \frac{\int S(\lambda) V(\lambda) \mathrm{d}\lambda \int S_\mathrm{c}(\lambda) R_\mathrm{D}(\lambda) \mathrm{d}\lambda}{\int S(\lambda) R_\mathrm{D}(\lambda) \mathrm{d}\lambda \int S_\mathrm{c}(\lambda) V(\lambda) \mathrm{d}\lambda}, \tag{3}$$

where I is the signal from the detector, R_v is the illuminance responsivity of the detector, $S(\lambda)$ is the relative spectral output of the source, $S_\mathrm{c}(\lambda)$ is the relative spectral output of the calibration source, and $R_\mathrm{D}(\lambda)$ is the relative spectral responsivity of the detector. [15]

2.3 Integrating sphere

An integrating sphere, also known as the Ulbricht sphere, is a hollow sphere that is used in luminous flux measurements in combination with a photometer. Theoretically, the inner surface of the sphere is coated with a perfectly diffusing material that does not have any spectral selectivity. All points on the sphere surface reflect the light to every other point in the sphere. Because of this, the illuminance at any point on the sphere surface consists of a direct beam of the light coming straight from the source and a sum of the reflected light from every other point on the surface. The illuminance measured at an opening on the sphere, when the direct light from the source is screened out, is proportional to the luminous flux of the source. [13]

For an ideal sphere the illuminance at any given point on the surface would be obtained by

$$E_\mathrm{v} = \rho \frac{\Phi_\mathrm{v}}{4\pi r^2(1-\rho)}, \tag{4}$$

where Φ_v is the total luminous flux of the internal source, ρ is the reflectance of the wall, and r is the radius of the sphere. Due to the non-idealities in the reflectance of the coating and the baffles, that screen out the direct light, the calculation of the luminous flux is not so straightforward and the luminous flux is obtained with comparison measurements. [13, 16]

2.3.1 Integrating sphere of Metrology Research Institute

The integrating sphere setup of MRI is shown as a photograph in Figure 4 and schematically in Figure 5. The sphere that has 1.65-m diameter is painted with highly reflecting, barium sulfate ($BaSO_4$) paint, that has approximately 98 % reflectivity with a nearly perfect diffuse reflectance over the visible wavelength range. [14, 17]

The MRI sphere has two sockets for interchangeable lamp holders, one at the top of the sphere and the other at the bottom. At the moment, two holders for E27 type lamps of different sizes, a new OLED holder [18] and a holder that can be attached to the bottom of the sphere for street light luminaire measurements are in use. The holders are designed so that the center of the lamp lies in the middle of the sphere. The unused attaching point on the sphere is tapped with a white cap.

The sphere has a port for the detector head (marked in Figure 5 with a), a port for the auxiliary lamp used in the self-absorption measurements (b), and an opening for the reference flux (c) produced by an external source. The first reflection of the flux from the external source on the sphere surface occurs at the reference point (d). $BaSO_4$ coated baffles are placed between all openings and the test-lamp. The positions of the baffles are shown in Figure 5.

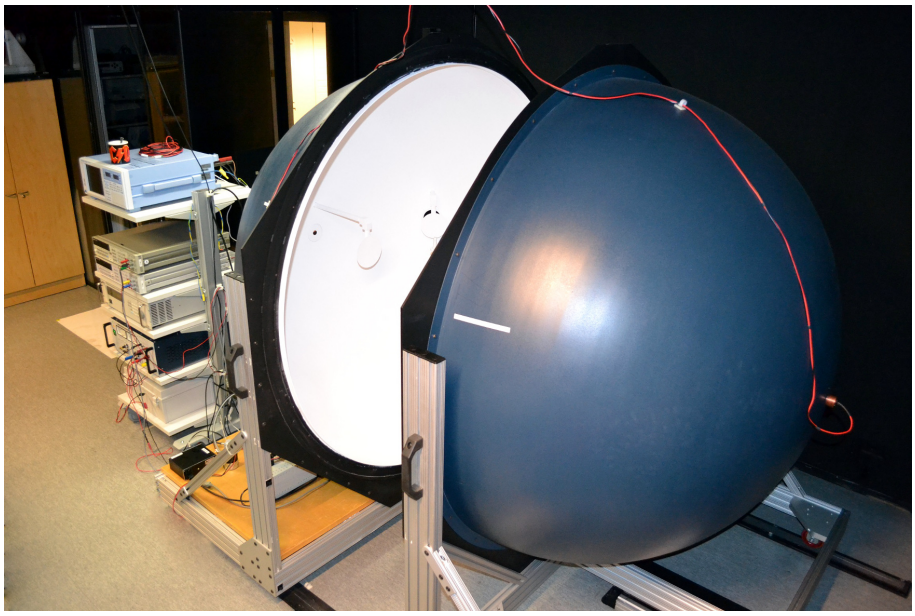

Figure 4: The integrating sphere at the MRI

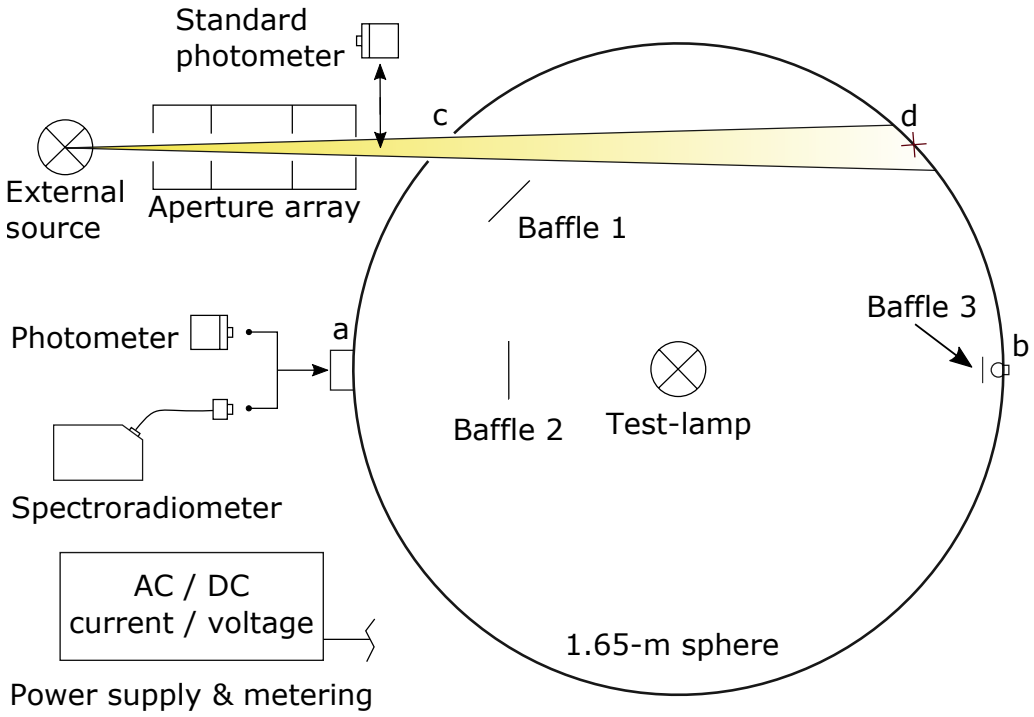

Figure 5: A schematical diagram of the integrating sphere setup.

The absolute integrating sphere method was developed [19] for measuring the luminous flux with high precision and to reduce the burning time of the lamps during the measurements as compared to goniophotometers. Before this method

the luminous flux was measured with goniophotometers rotating either the detector around the lamp or the lamp around its center. Rotating the measured lamp may cause an error to the results if the lamp is sensitive to the burning position.

In the absolute integrating sphere method a detector attached to the sphere measures first the signal produced by the flux of the external reference source Y_{ext}. After that, the external source is blocked, the source inside the sphere is turned on, and the signal produced by the source Y is measured. The luminous flux of the internal source is calculated by

$$\Phi_{\text{v}} = \Phi_{\text{ext}} \frac{Y}{Y_{\text{ext}}}, \tag{5}$$

where the reference flux of the external source Φ_{ext} in absolute integrating sphere method is calculated from the average illuminance E_{ext} of a standard lamp limited by a precision aperture with an area A_{ext},

$$\Phi_{\text{ext}} = E_{\text{ext}} A_{\text{ext}}. \tag{6}$$

2.3.2 Correction factors of the absolute integrating sphere method

The variation in the reflectivity of the sphere surface and non-uniformity produced by features of the sphere, such as sphere seam, ports and baffles, and the configurational differences when measuring the flux of the external and internal source introduce a need for several correction factors to correct the non-idealities of the measurement setup. The combination of correction factors used for correcting the results is

$$f = \frac{k_{\text{int}} c_{\text{i}} k_{\text{a}} \alpha}{k_{\text{ext}} c_{\text{e}} \beta}, \tag{7}$$

where k_{int} is the spatial non-uniformity correction of the internal source, k_{ext} is the spatial non-uniformity correction for the external source at the reference point, c_{e} is the color correction for the external source and c_{i} for the internal source, k_{a} is the illuminance uniformity of the external source at the aperture plane, α is the self-absorption correction and β is the correction for the angle of incidence. [14, 19]

At the MRI, the spatial responsivity distribution function (SRDF) of the sphere is measured using a commercial integrating sphere scanner [20] (shown in Figure 6). The scanner that can be connected to the E27 lamp socket of the sphere has two stepper motors to rotate the light beam of the scanner to any direction on the sphere surface. One of the motors rotates the beam 180° horizontally and the other one 360° vertically in the sphere. Sphere scanner is connected to a controller with two-wire connection that sends commands to the motors and powers the LED and the fan for cooling the LED. The controller is operated with a LabVIEW-program developed at the MRI.

Normalized spatial responsivity distribution function is calculated from the scanning results by

$$K^*(\theta_n, \phi_m) = \frac{4\pi K(\theta_n, \phi_m)}{\sum_{n=1}^{N} \sum_{m=1}^{M} K(\theta_n, \phi_m) f(\theta_n) \Delta\phi}, \tag{8}$$

Figure 6: The scanner attached to the sphere pointing towards the baffle of the reference port. The detector port with its baffle is seen on the left.

where θ and ϕ are the vertical and horizontal angles of the measured point on the sphere surface respectively, N and M are the number of points in vertical and horizontal directions and $K(\theta_n, \phi_m)$ is the matrix containing the measured relative signals at different directions in the sphere. The weighting factor of the spherical coordinate system is calculated by

$$f(\theta_n) = \begin{cases} \cos(\theta_n) - \cos(\theta_n + \frac{\Delta\theta}{2}) & \text{if } n = 1 \\ \cos(\theta_n - \frac{\Delta\theta}{2}) - \cos(\theta_n + \frac{\Delta\theta}{2}) & \text{if } 2 \leq n \leq N-1 \\ \cos(\theta_n - \frac{\Delta\theta}{2}) - \cos(\theta_n) & \text{if } n = N \end{cases}. \tag{9}$$

The spatial non-uniformity correction for an internal source can be calculated using the normalized SRDF by

$$k_{\text{int}} = \frac{\sum_{n=1}^{N}\sum_{m=1}^{M} I_{\text{rel}}(\theta_n, \phi_m) f(\theta_n) \Delta\phi}{\sum_{n=1}^{N}\sum_{m=1}^{M} K^*(\theta_n, \phi_m) I_{\text{rel}}(\theta_n, \phi_m) f(\theta_n) \Delta\phi}, \tag{10}$$

where $I_{\text{rel}}(\theta_n, \phi_n)$ is the relative intensity distribution of the internal lamp. For incandescent lamps the correction factor is close to unity. For OLEDs and other types of sources with non-isotropic radiation pattern, k_{int} can differ significantly from unity. [21]

The spatial non-uniformity correction for the external flux is calculated by

$$k_{\text{ext}} = \frac{1}{K^*(\theta_{\text{ref}}, \phi_{\text{ref}})}, \tag{11}$$

where θ_{ref} and ϕ_{ref} refer to the point on the sphere surface where the first reflection of the reference flux occurs (d in Figure 5).

The color corrections for the internal and external sources c_{i} and c_{e}, respectively, are calculated similarly as the correction factor for the non-ideality of the spectral responsivity of the photometer (Equation 3). The correction for the internal source is calculated by

$$c_{\mathrm{i}} = \frac{\int S_{\mathrm{i}}(\lambda)V(\lambda)\mathrm{d}\lambda \int R_{\mathrm{s}}(\lambda)S_{\mathrm{A}}(\lambda)\mathrm{d}\lambda}{\int S_{\mathrm{A}}(\lambda)V(\lambda)\mathrm{d}\lambda \int R_{\mathrm{s}}(\lambda)S_{\mathrm{i}}(\lambda)\mathrm{d}\lambda} \tag{12}$$

where the spectral responsivity of the integrating-sphere photometer $R_S(\lambda)$ is obtained by multiplying the relative spectral response of the photometer $R_{\mathrm{D}}(\lambda)$ and the throughput of the sphere $T(\lambda)$. $S_{\mathrm{i}}(\lambda)$ is the spectrum of the internal source and $S_{\mathrm{A}}(\lambda)$ is the spectrum of the CIE Standard Illuminant A, which is defined as a Planckian radiator at a temperature of 2856 K. The correction factor for external source c_{e} is calculated by replacing the spectrum of the internal source $S_{\mathrm{i}}(\lambda)$, with the one of the external source $S_{\mathrm{e}}(\lambda)$. [14, 22]

In this work the luminous flux responsivity of the sphere was measured only once for the empty sphere with the external source, as opposed to separately to each OLED, to minimize the burning time of the external standard source. To correct the difference of the configuration between the luminous flux responsivity and the OLED measurements, separate self-absorption measurements were carried out with the auxiliary lamp for each OLED. The self-absorption correction factor is calculated as a ratio of the measurement signals when the OLED is in the sphere attached to the holder S_{DUT} and when the sphere is empty S_{empty} by

$$\alpha = \frac{S_{\mathrm{empty}}}{S_{\mathrm{DUT}}}. \tag{13}$$

In the case of measuring the luminous flux responsivity of the sphere separately for each OLED, the self-absorption is not used.

2.4 Goniospectrometer for OLED measurements

The goniospectrometer setup (Figure 7) is used for measuring the angular distribution of a light source. The goniometer consists of two motorized rotary stages, a stray-light protection box and a spectroradiometer.

The two rotary stages are installed on an optical table so that one has the optical axis (OA) as a rotation axis and the other one rotates about an axis, which is perpendicular to the optical axis in the vertical direction. The optical axis goes through the centers of the apertures on the stray-light box. The light source is mounted on the goniometer and rotated about the horizontal and vertical axes to measure the intensity distribution in different directions. Placing the sample on the intersection of the two rotation axes is accomplished by using a manual linear translator on z-axis. Knife-edge apertures with different diameters can be attached to the stray-light box. The Konica Minolta CS-2000A with the diffuser attachment was used to measure the relative intensity distribution of the light source. A typical

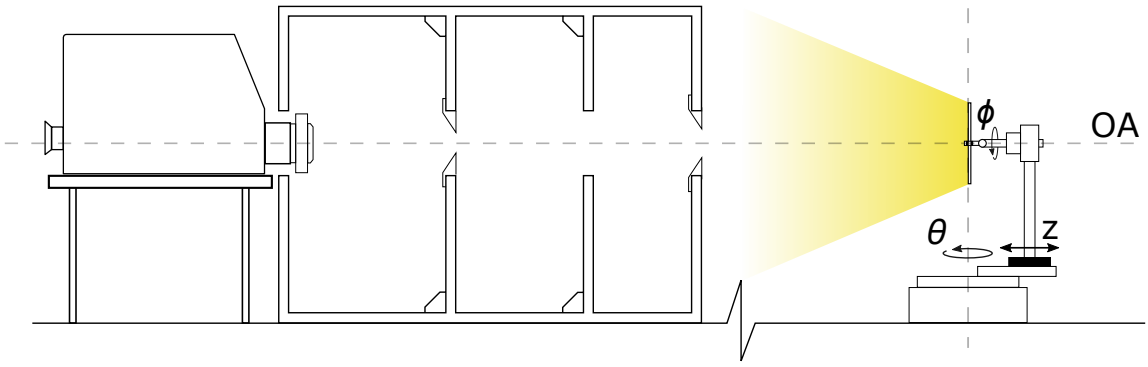

Figure 7: Goniospectrometer setup at MRI

duration of the measurement of the angular distribution $I_{\text{rel}}(\theta, \phi)$ of an OLED is around 3.5 hours.

None of the OLEDs measured in this thesis produced significant back-emission. For this reason only one hemisphere of the samples was scanned. In case of OLEDs with back-emission, the reflections from the holder structure should be taken into account.

In addition to measure the radiation pattern of OLEDs and E27 retrofitted SSL lamps, the system can also be used for measuring the beam characteristics of the integrating sphere scanner, edge-emission of OLEDs, and angular distribution of a diffuser head. The measurement distance can be also changed by moving the goniometer on the optical table.

2.5 Detectors for optical measurements

2.5.1 Photometer heads

Photometer is a broadband detector whose spectral responsivity is close to the $V(\lambda)$ filter. The photometers used in this work, LM-1 and HUT-1 (Figure 8), are photodiode-based commercial photometers by PRC Krochmann. LM-1 and HUT-1 are illuminance-measuring photometers with temperature controlled V(λ) filters and circular apertures with a diameter of 8 mm. The filtered radiant energy is converted to electrical current with silicon photodiode, Hamamatsu S1227. The photocurrent of the detectors in typical measurements is between 1 nA and 500 μA.

LM-1 has a planar diffuser with a precise cosine response as the entrance optics to collect radiation at wider range of incident angles. HUT-1 is not equipped with a diffuser and thus has a limited viewing angle. LM-1 is used as a measurement photometer in the integrating sphere setup to measure the signal over a wide solid angle, and not just a reflection from the baffle in front of the detector port. HUT-1 is used for measuring the illuminance of the external source. [14]

Figure 8: Photometer heads LM-1 and HUT-1 used in the measurements with the integrating sphere.

2.5.2 Spectroradiometers

For this thesis, two type of spectroradiometers were used, one scanning, Bentham DTMc300, and two photodiode array spectroradiometers, Ocean Optics QE65 Pro and Konica Minolta CS-2000A. The used photodiode array spectroradiometers are shown in Figure 9.

In an array spectroradiometer light is dispersed on diffraction grating to spectral components, and after that, the light is focused to the photodiode array using lenses or mirrors. In a scanning spectroradiometer the grating is rotated so that every wavelength is measured separately by a single detector, and thus the measurement takes more time.

The CS-2000A has an array of 512 elements with Peltier cooling for reducing the signal-to-noise ratio (SNR). The wavelength range of the device is from 380 to 780 nm with display wavelength bandwidth of 1.0 nm. The wavelength precision according to the specifications is ±0.3 nm and the spectral bandwidth is 5 nm or less. The instrument performs an automatic dark signal measurement using an internal shutter. Due to this no manual dark signal measurement is needed. The integration time for the device ranges from 5 ms to 120 seconds. The instrument has an attachable diffuser with diameter of 25 mm for measuring spectral irradiance and illuminance of a light source. [23]

The QE65 Pro has a Hamamatsu CCD array as a detector with a wavelength range of 200–1100 nm. The detector is thermoelectrically cooled and the minimum temperature it can reach is 40 °C below ambient temperature. The optical resolution of the device is 1.58 nm with the installed grating and the used entrance aperture. Integration time of the device ranges from 8 ms to 15 minutes. A diffuser head is attached to the device with an optical fiber that has numerical aperture of 0.22. The transmission of the fiber is optimized on a wavelength range from 400 nm to

Figure 9: On the left is the Ocean Optics QE65 Pro with the Bentham D7 type diffuser and on the right side is Konica Minolta CS-2000A with the diffuser attached as entrance optics.

2100 nm. Signal from the device is read as counts on the computer. The output signal saturates close to 60 000 counts and this needs to be taken into account when selecting the integration time for the measurements. [24]

The DTMc300 is a double monochromator spectroradiometer. A cooled photomultiplier tube is used as a detector in the visible wavelength range. Bentham D7 type diffuser is connected to the monochromators with a 2-meter fiber bundle. A typical measurement over the visible wavelength range with the instrument usually takes half an hour or more. Because the time of the spectral measurement is over one decade larger than measurement made with an array spectroradiometer, the scanning spectroradiometer is not suitable for the spatial scan of the integrating sphere. [25]

3 Technical improvements for spectral scanning of the sphere

In this chapter, the improvements of the luminous flux measurement setup are discussed. In order to reduce the aqcuisition time in the spectral measurement, and thus make spectral scanning of the spatial uniformity of the integrating sphere viable, a new diffuser head with high throughput was developed. In addition the LED-based sphere scanner was modified to increase the usable wavelength range of the spatial uniformity data. These modifications are detailed and discussed in this chapter.

3.1 New diffuser for spectroradiometer measurements

In preliminary tests the transmission of the current Betham D7 type diffuser head of the spectroradiometer QE65 Pro was viewed as a limiting factor. Increasing the integration time to the needed level was not seen as an option because the time used for scanning the whole sphere would have gone up to several days. Measurements showed that with the existing diffuser, only 42 percent of the dynamic range of the spectroradiometer could be used in the sphere scanning that takes, in total, up to 24 hours. A new diffuser head for the integrating sphere measurements was developed to increase the signal reaching the spectroradiometer in the spectral scan of the integrating sphere.

Various diffuser samples with diameter of 15 mm (Figure 10) were chosen for test measurements. The tested samples were all made of quartz that has gas "bubbles" inside them to achieve the diffusion. The angular and transmission properties of the material have been studied at the MRI earlier. [26]

Figure 10: The new MD01 diffuser (top-right) and tested 15-mm diameter diffuser samples.

Mechanics of the diffuser were designed in such way that the new diffuser could be used with the existing integrating sphere adapter of the D7 diffuser. The distance between the inner surface of the diffuser and the optical fiber entrance was set to 40 mm to ensure that the field of view of the optical fiber covers the entire visible

area of the diffuser. The diffuser body was manufactured of aluminum and anodized to black. The design of the developed diffuser mechanics is shown in Appendix A.

All of the diffuser samples were characterized attached to the diffuser mechanics in a modified goniospectrometer setup using a light emitting diode as the light source. The measurement distance was set to 60 cm from the front surface of the diffuser. The diffuser was rotated from -90° to 90° in 2.5° steps horizontally. This measurement sequence was repeated for different azimuth angles (0°, 45°, 90° and 135°). Dark signal was measured before and after each sequence.

Two different selection methods were used. First one compares the transmitted light of the new diffuser to the D7 diffuser and the second views the quality index f_2, that describes the difference of the angular response of a diffuser to a cosine response relatively. The f_2 value is calculated for every azimuth angle ϕ by

$$f_2(\phi, \lambda) = \int_{0°}^{85°} |f_2(\varepsilon, \phi, \lambda)| \sin 2\varepsilon \mathrm{d}\varepsilon, \tag{14}$$

where

$$f_2(\varepsilon, \phi, \lambda) = \frac{R_\mathrm{S}(\varepsilon, \phi, \lambda)}{R(0, \phi, \lambda)\mathrm{S} \cos \varepsilon} - 1. \tag{15}$$

The spectral output of the detector ${}_R\mathrm{S}(\varepsilon, \phi, \lambda)$ is presented as a function of the angle of incidence ε and the azimuth angle ϕ. [27, 28]

The results from the measurements are shown in Table 3. The f_2 value is calculated as an arithmetic mean of the spectral f_2 values between wavelengths 450–700 nm. The measured f_2 value of the D7 type diffuser is significantly larger than the photometrically earlier measured value at the MRI. This is most probably due to the noise at lower signal levels in the measurements.

Table 3: Transmission and f_2 value of different diffusers. Transmission is reported relative to the transmission of the D7 diffuser

Sample	Thickness	Normalized transmission	f_2
D7		100 %	1.23 %
Sample 1	1 mm	166 %	16.5 %
Sample 1	2 mm	124 %	4.24 %
Sample 2	1 mm	64 %	8.01 %
Sample 2	2 mm	40 %	6.10 %
Sample 3	2 mm	93 %	5.19 %

The diffusers Sample 2 and 3 have lower transmittance than the D7 diffuser for all the tested thicknesses. Sample 1 with thickness of 2 mm has 24 % larger transmittance than D7 and the f_2 value is larger by the factor of 3.5. Sample 1 with 1 mm thickness has over 60 % increase in transmittance when compared to D7. The angular response of this diffuser is poor, which means that utilizing it in measurements, which rely on good cosine response is not possible. However as cosine response is not ideally needed in detectors that are used in integrating sphere

measurements, this sample was chosen as the diffuser element for the new detector head, due to its high transmittance.

The cosine error of the ready diffuser, hereafter referred to as MD01 (shown in Figure 10), calculated at wavelength range of 600–620 nm is shown in Figure 11. The spectral f_2 value shown in Figure 12 suggests that the diffuser may have spectral selectivity.

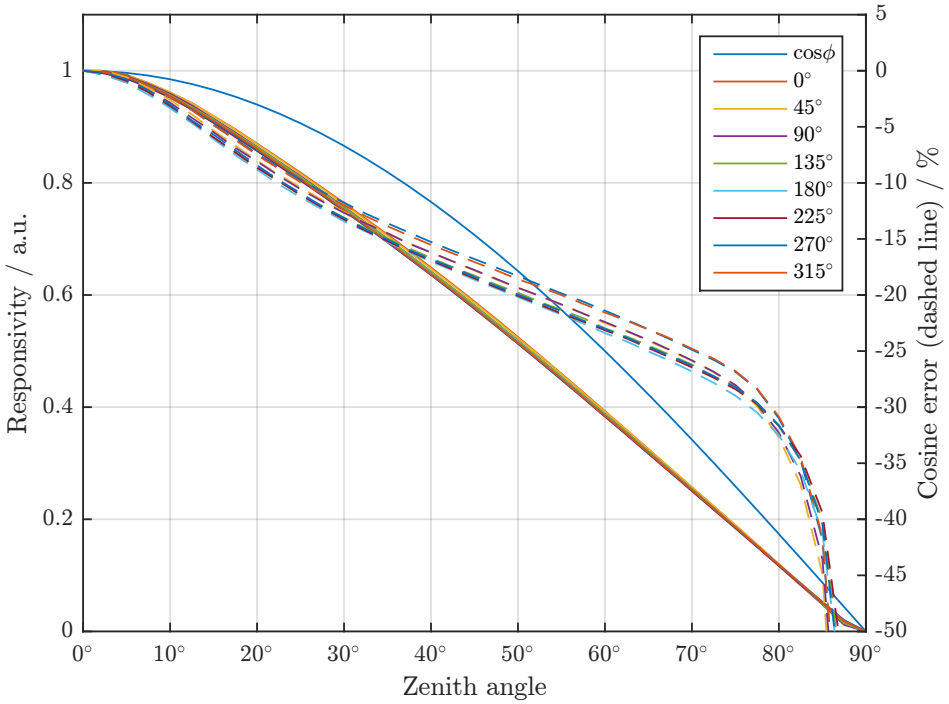

Figure 11: The relative responsivity as a function of incident angle and cosine error of the MD01 diffuser. The different curves are for the rotation around the optical axis.

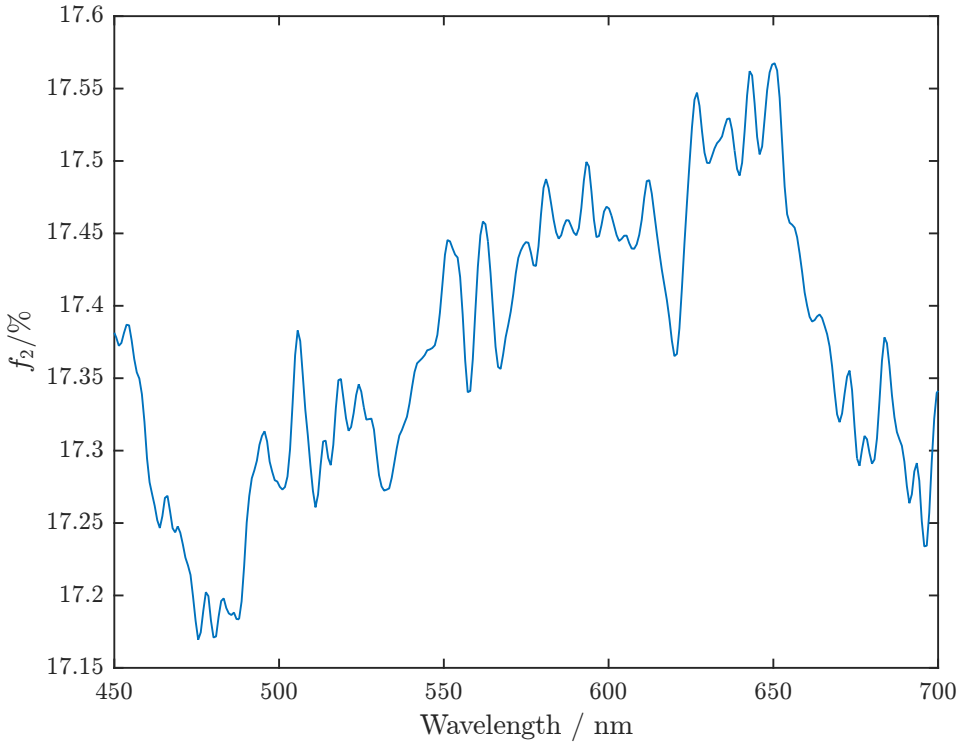

Figure 12: Directional quality index f_2 measured for the MD01 diffuser head as a function of wavelength.

3.2 Integrating sphere scanner

The optical parts of the sphere scanner are shown in Figure 13. The tube for directing the light beam in the sphere is fastened to the LED housing using a thread. The lens, utilized for focusing the beam, is tightened to the housing by pressing it against the LED with the aluminum ring shown in the figure. The original LED was removed from the housing to compare it with other LEDs.

The change of the original cold white (6300 K) high power LED in the sphere scanner to a warm white LED was studied, because of the advantage of a wider spectral distribution in the planned spectral spatial scan of the integrating sphere. In order to find the best LED for the purpose, four different warm white (2700–3200 K) light emitting diodes from four different manufactures were chosen for further study. The LEDs and their measured correlated color temperatures are presented in Table 4. Two separate sets of these LEDs were aged for 150 hours and their spectral irradiances were measured before and after the ageing to study their long term stability. The width of the wavelength range over which the SNR was seen sufficient for the spectral scan of the integrating sphere, was used as the criterion for choosing the new warm white LED.

The LEDs were measured with Konica Minolta CS-2000A using the 25 mm diffuser attached to it. The measurement distance from the diffuser was set to 10 cm and all the LEDs were operated with the maximum current of the scanner, 700 mA. In Figure 14 are shown the spectral irradiances of the original cold white LED and

Figure 13: Optical parts of the integrating sphere scanner opened for the change of the LED.

the tested warm white LEDs before and after the ageing of 150 hours. It can be seen that the irradiance level at the phosphor peak is approximately 5 % lower after the ageing for all the tested light emitting diodes.

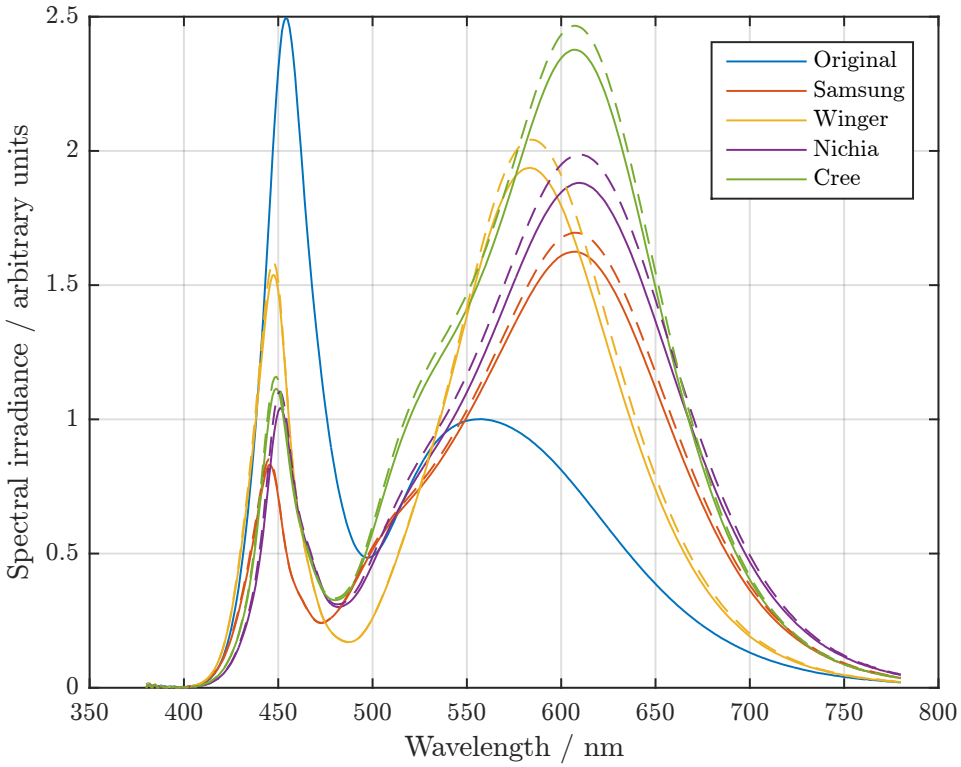

Figure 14: Original LED of the sphere scanner and proposed warm white replacement LEDs before (dashed line) and after (solid line) after an ageing period of 150 hours.

The spatial scan of the integrating sphere with the original cold white LED

shows that at 700 nm the spectroradiometer counts are approximately 5 % of the saturation level of the spectroradiometer with an integration time of 20 s. At this signal level, the spatial features of the integrating sphere are lost in noise, and the spatial correction cannot be calculated. The measured irradiance at the wavelength of 700 nm was 0.0085 W/m^2 for the original source as can be seen from Table 4. With three of the tested LEDs the irradiance was larger than this even at 735 nm. Based on the analysis the Nichia LED improves the situation the most at the red end of the spectrum and it was installed to the integrating sphere scanner.

Table 4: Measured correlated color temperatures (CCT), phosphor peak positions and spectral irradiance levels at the phosphor peak and 700 nm for original LED in the sphere scanner and tested warm white light emitting diodes

LED	CCT	Phosphor peak	E_e@ peak	E_e@ 700 nm
Original	9040 K	557 nm	0.065	0.0085
Winger	3210 K	584 nm	0.106	0.0236
Samsung	2850 K	607 nm	0.126	0.0124
Nichia	2760 K	610 nm	0.122	0.0304
Cree	2830 K	607 nm	0.155	0.0262

The stability of the integrating sphere scanner with the new warm white LED was studied using the photometer LM-1. The scanner was monitored inside the integrating sphere for a total of 5 hours. The standard deviation of the measured signal over the measurement period of 30 minutes was 0.012 % 5 minutes after switching the source on and 0.013 % after 3 hours of stabilizing (Figure 15a). From the figure it is seen that the signal differs at most 0.035 % from the value at the beginning of the half an hour time frame. Based on the results it can be concluded that the stability of the LED is sufficient for scanning the integrating sphere and a stabilization time of 10-15 minutes before starting the measurement sequence is adequate.

The profile of the scanner beam was measured in the goniometer. In the measurement, the tube of scanner was rotated while QE65 Pro was used as the detector. The rotation in the measurements was about the center of the open end of the tube. The scanner was rotated from -45° to 45° in 1° steps. The effect of the signal level outside this region on the integrated spectrum of the beam was negligibly small. The scanner was measured at different azimuth angles (0°, 45°, 90° and 135°). The spectral shape of the beam is shown in Figure 15b.

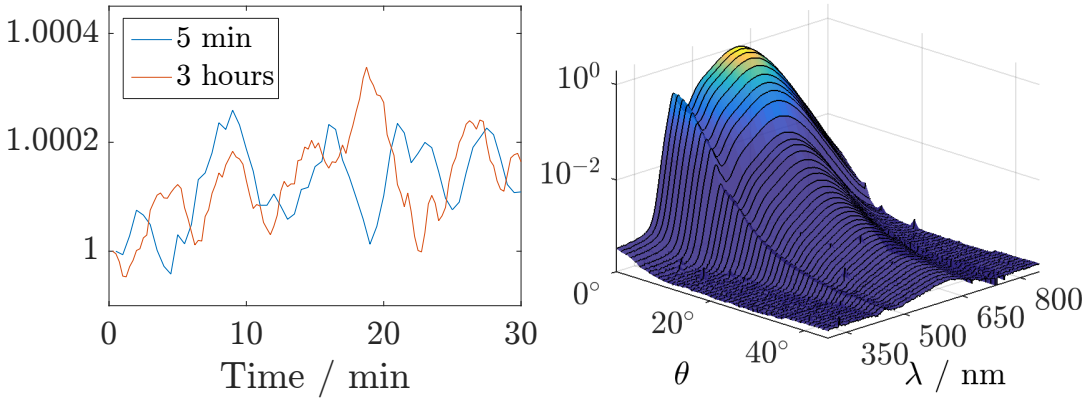

(a) (b)

Figure 15: In Figure (a) the stability of luminous flux of the integrating sphere scanner relative to the beginning of the sequence with different stabilization times is shown after changing the LED. In (b) is the spectral shape of the angular distribution of the light beam of the sphere scanner measured with QE65 Pro.

4 Characterization of the integrating sphere

In this chapter, the results of the characterization of the integrating sphere setup at the MRI are presented. Differences of the SRDF before and after the modification of the measurement equipment are studied, the photometric and spectral spatial maps are compared, and the responsivity of the sphere at different wavelengths is examined. Also the spectral throughput of the integrating sphere, needed for the spectral mismatch corrections, is measured using different methods. In addition, the correction factor of the illuminance uniformity of the external source k_a is measured and analyzed in a new, improved way.

4.1 Scanning of the spatial uniformity of the sphere spectrally and with a photometer

The integrating sphere at the MRI was scanned with the upgraded sphere scanner and spectroradiometer Ocean Optics QE65 Pro with the new MD01 diffuser. The integrating sphere was also scanned photometrically using the photometer LM-1. These results were compared to the measurement results that were carried out with the cold white LED of the scanner and the photometer LM-1.

During the spatial scan, the surface of the sphere is scanned from bottom of the sphere vertically to the top of the sphere and after that, continued straight to the other side of the sphere without changing the horizontal angle. The sequence is repeated for every horizontal angle. The measurement of one 360° vertical section takes less than one hour using the QE65 Pro spectroradiometer with integration time of 30 seconds. In case of LM-1, less than 10 minutes is needed for measuring one vertical slice. The map of the SRDF is calculated from the measurement results using Equation 8.

The map of the SRDF of the sphere measured using the photometer is shown in Figure 16. From the map the detector {90° , 180°}, the reference {90° , 225°} and the auxiliary {90° , 0°} ports, the seam of the two halves of the sphere (horizontal angles 90° and 270°) and the cap covering the lamp holder socket {15° , 180°} on the bottom can be seen clearly. Due to the increased signal level, the SNR was improved by 14 % when compared to the measurements made with the original cold white LED of the scanner.

The difference of two different sphere maps can be calculated using equation

$$K^*_{\text{diff}}(\theta_n, \phi_n) = 1 - \frac{K^*_1(\theta_n, \phi_n)}{K^*_2(\theta_n, \phi_n)}. \tag{16}$$

From the difference map a RMS value (root-mean-square) is calculated by

$$K^*_{\text{RMS}} = \frac{\sqrt{\sum_{n=1}^{N}\sum_{m=1}^{M} K^*_{\text{diff}}(\theta_n, \phi_m)^2 f(\theta_n)}}{M\sum_{n=1}^{N} f(\theta_n)}, \tag{17}$$

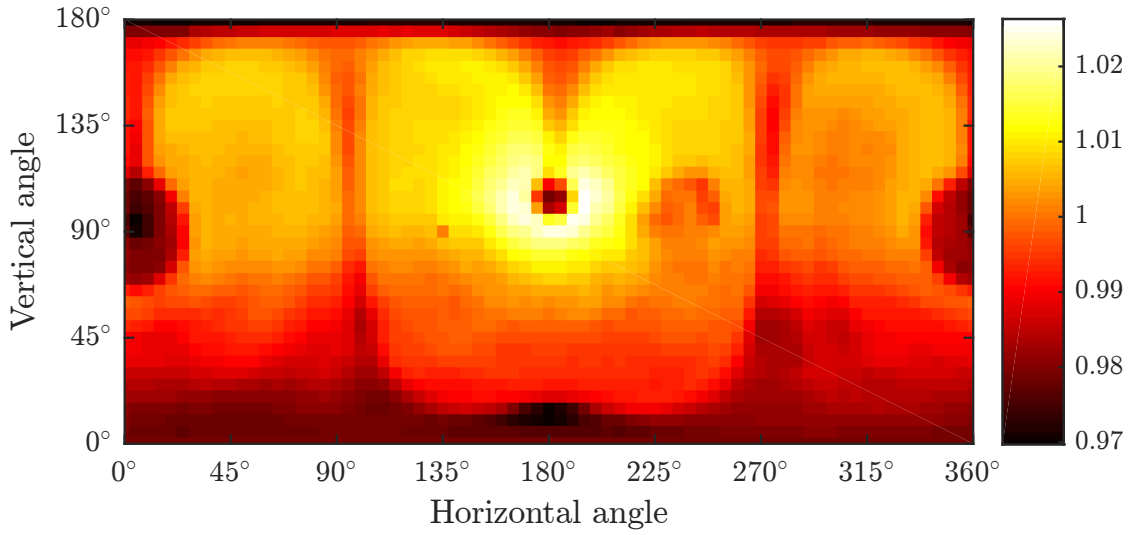

Figure 16: Normalized SRDF of the integrating sphere, measured using photometer LM-1.

where $f(\theta_n)$ is defined by Equation 9. For analyzing the effect of the differences between the maps on the correction coefficient, spatial correction k_{comp} is calculated for a virtual internal source that radiates to one hemisphere, has a Lambertian angular distribution, and is pointing towards the bottom of the sphere. Furthermore, the spatial correction for the external correction is used for comparing the differences of the maps.

Figure 17 shows the difference of the maps scanned with LM-1 before and after changing the warm white LED to the scanner. The calculated k_{comp} before and after the modification are very similar to each other 1.0077 and 1.0079, as are the correction factors for the external source k_{ext} with values of 0.9967 and 0.9984 respectively. The RMS value for the difference map is 0.062 %. Differences between the scans of up to 4 % at points in the sphere where the baffles are located or where the two halves of the sphere are joined are most likely explained by the repeatability of alignment when attaching the scanner to the sphere.

The difference of the scans measured with the photometer LM-1 and the spectroradiometer QE65 Pro with the new diffuser MD01 is shown in Figure 18. The measurements were performed without removing the scanner from the sphere. Because of this, the repeatability of the alignment is not an issue and the difference map shows how the selection of the measurement device affects the end result. Even though the difference is at some points over 1 % the RMS difference in the whole sphere is 0.045 %. The k_{comp} value for the map measured with spectroradiometer is 1.0075 as compared to 1.0079 of the photometer measurement. The value k_{ext} for the map measured using the MD01 is 0.9957 and the RMS-value 0.045 %. The most probable explanation for the difference viewed at the detector and auxiliary ports is the difference in the angular response between the LM-1 photometer and the MD01 diffuser head.

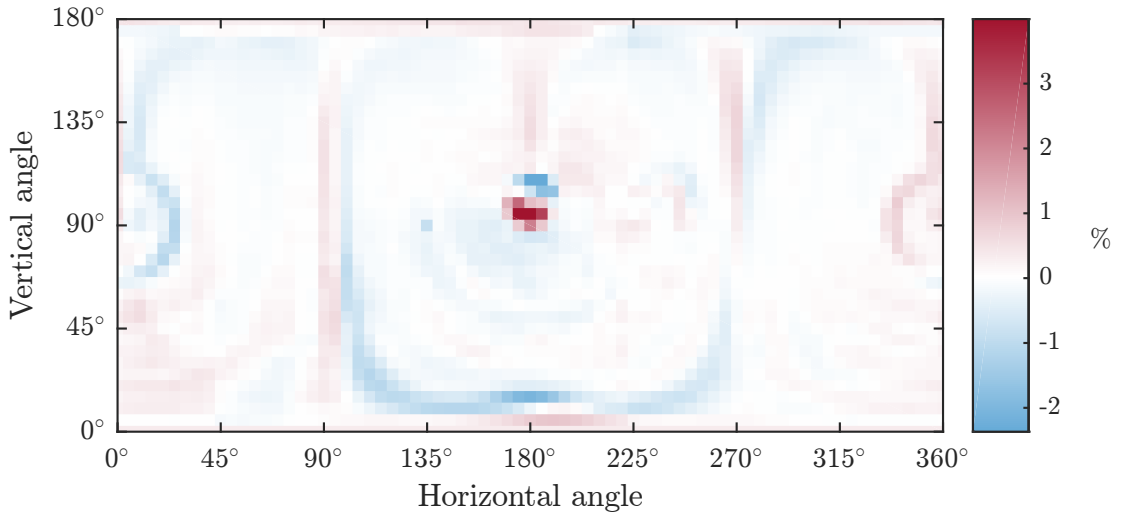

Figure 17: Difference of the sphere scans before and after the changing the LED of the sphere scanner, RMS 0.062 %.

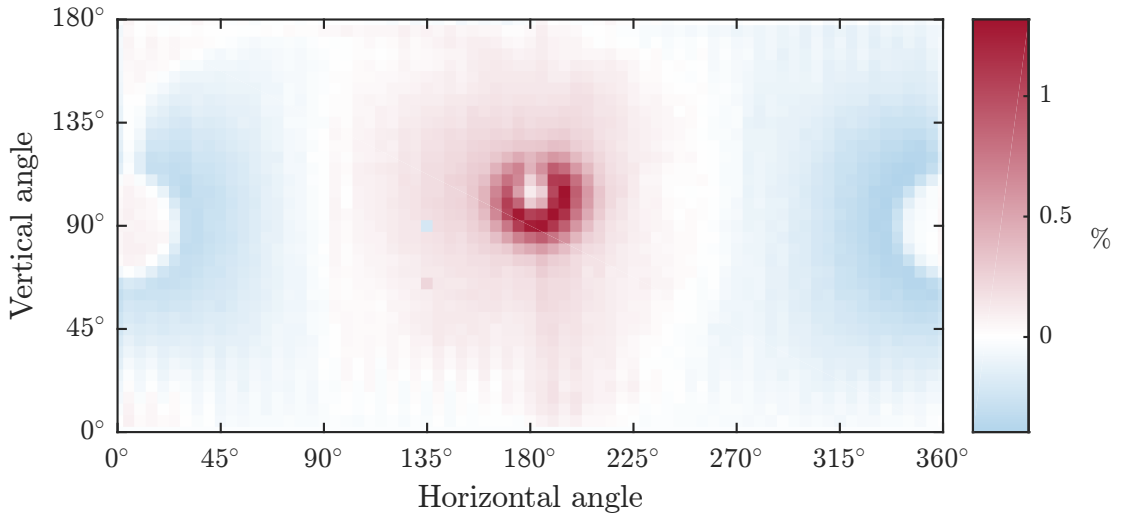

Figure 18: Difference of the normalized SRDF measured with LM-1 and QE65 Pro with the MD01, RMS 0.045 %.

Difference of the spatial maps of the sphere at the the full-width-at-half-maximum wavelengths (546 nm and 671 nm) of the phosphor peak is shown in Figure 19. The difference is calculated so that the map of the longer wavelength is used as $K_1^*(\theta_n, \phi_m)$ in the Equation 16 and the lower as $K_2^*(\theta_n, \phi_m)$. The map shows over 0.5 % difference between the top and the bottom of the sphere. The calculated k_{comp} values are 1.0079 and 1.0065 for wavelengths 546 nm and 671 nm, respectively, meaning the bottom of the sphere has 0.15 % lower spatial correction at 671 nm compared to 546 nm.

The difference map of the blue (450 nm) and the phosphor (612 nm) peaks is shown in Figure 20. The k_{comp} values for the peaks are 1.0097 and 1.0071 and the

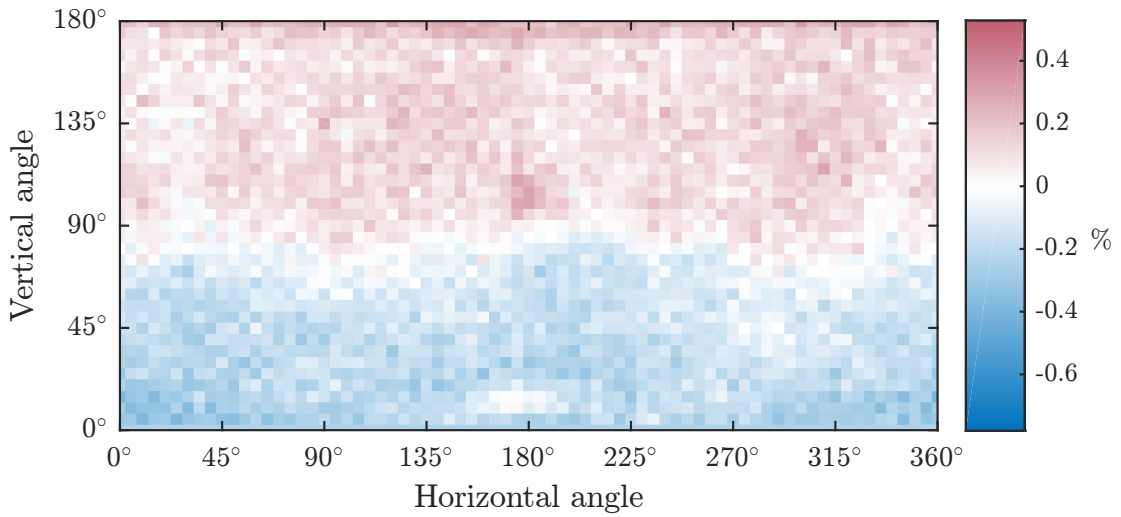

Figure 19: The difference of the spatial maps at wavelengths 546 nm and 671 nm, RMS 0.023 %.

spatial correction for the bottom of the sphere is 0.26 % lower for the phosphor peak when compared to the blue peak. In this case the variation in the difference map between the bottom and the top of the sphere is up to 1 %.

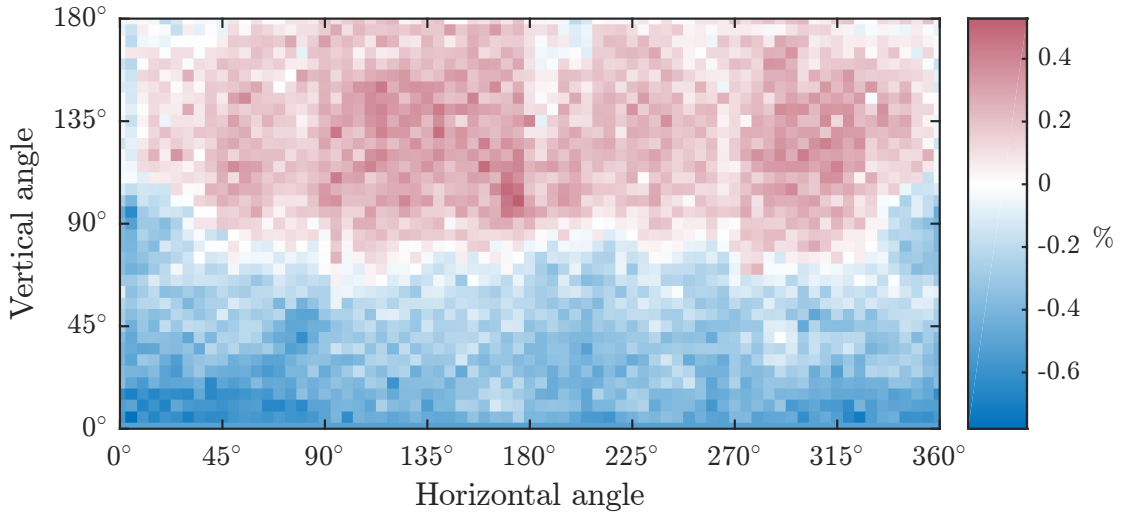

Figure 20: The difference of the spatial maps at the blue (450 nm) and the phophor (612 nm) peaks, RMS 0.042 %.

The spectral value for the the spatial correction of the virtual source k_{comp} at wavelength range from 380 to 780 nm is shown in Figure 21. The spatial correction has quite constant negative slope at wavelengths over 400 nm. If the virtual source is pointing towards the top of the sphere instead of the bottom, similar but positive slope is seen. Based on this knowledge, the spectral characteristics of spatial corrections of

real OLEDs should change as a function of the orientation of the panel.

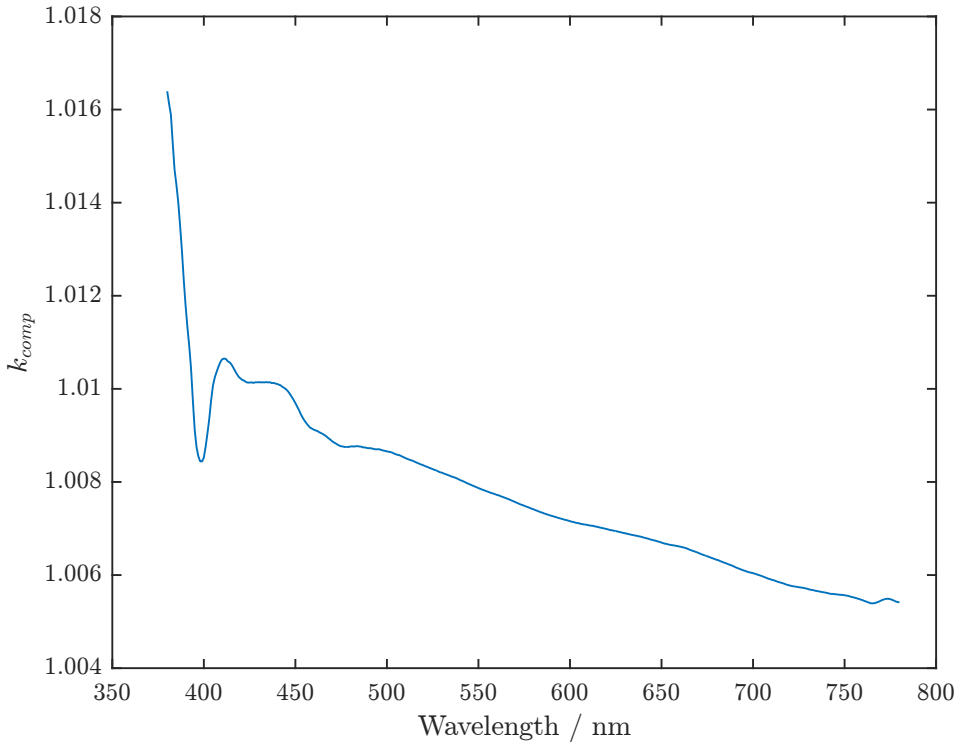

Figure 21: The spectral spatial correction for an imaginary internal source that radiates to one hemisphere, has perfect Lambertian radiation pattern, and is pointing towards the bottom of the integrating sphere.

The spectral spatial correction coefficient k_{ext} is shown in Figure 22. The graph has significant noise that is a result of the definition of the coefficient, as only one measurement point on the sphere is used. The measurement program shoud be modified to measure the reference point after every vertical slice to decrease the noise in the spatial correction k_{ext}.

4.2 Spectral throughput of the integrating sphere

In order to measure the spectral radiant flux of a lamp in the integrating sphere, the relative spectral throughput of the sphere needs to be known. In photometric measurements, the spectral throughput of an integrating sphere is used for calculating the spectral mismatch correction.

The throughput of the integrating sphere was measured with two different methods. The first and previously used method relies on measuring a tungsten reference lamp with a known spectral irradiance. In this work an Osram WI40 Globe lamp was used for the measurements. The spectral irradiance of the lamp was first measured in three different directions on an optical rail with a spectroradiometer and the arithmetic mean of the results was used as the spectral irradiance in the analysis. After that the lamp was measured in the integrating sphere using the same instrument. The

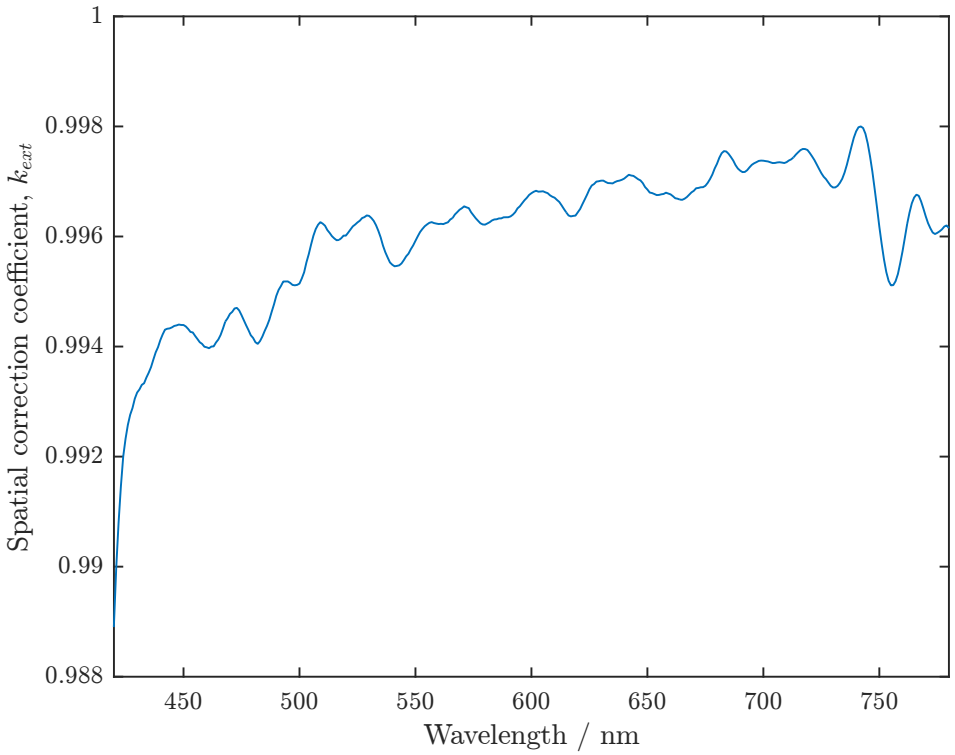

Figure 22: The spectral spatial correction for the external source k_{ext} at the wavelength range of 430–780 nm.

spectral throughput is defined as

$$T(\lambda) = \frac{E_{\text{in}}(\lambda)}{E_{\text{out}}(\lambda)} \frac{E_{\text{out}}(555\text{ nm})}{E_{\text{in}}(555\text{ nm})}, \tag{18}$$

where $E_{\text{out}}(\lambda)$ is mean of three measurements on optical rail from different directions and $E_{\text{in}}(\lambda)$ is measured inside the sphere. These measurements were carried out using the Bentham DTMc300 and the Ocean Optics QE65 Pro spectroradiometer with the new MD01 diffuser attached to it.

In the second method, the spectral spatial scan of the sphere and measurement of the scanner beam are used to determine the spectral throughput of the sphere. The spectroradiometer does not need to be calibrated provided that the same instrument is used in both the spatial scan and characterizing the scanner beam. The spectral throughput is calculated by

$$T(\lambda) = C \frac{\sum_{n=1}^{N} \sum_{m=1}^{M} K(\theta_n, \phi_m, \lambda) f(\theta_n) \Delta\phi}{2\pi \sum_{l=1}^{L} I_{\text{rel}}(\theta_l, \lambda) f(\theta_l) \Delta\phi}, \tag{19}$$

where $I_{\text{rel}}(\theta_l, \lambda)$ is the spectral angular distribution of the beam of the sphere scanner that was measured in Section 3.2 and C is to normalize the throughput to unity at

555 nm. Because of the different signal levels in the measurement of the beam and of the responsivity of the integrating sphere, different integrating times were used in them. Due to this the linearity of the measurement instrument was measured with integrating times from 0.3 up to 30 seconds, and the results of the throughput were corrected for the linearity in integration time.

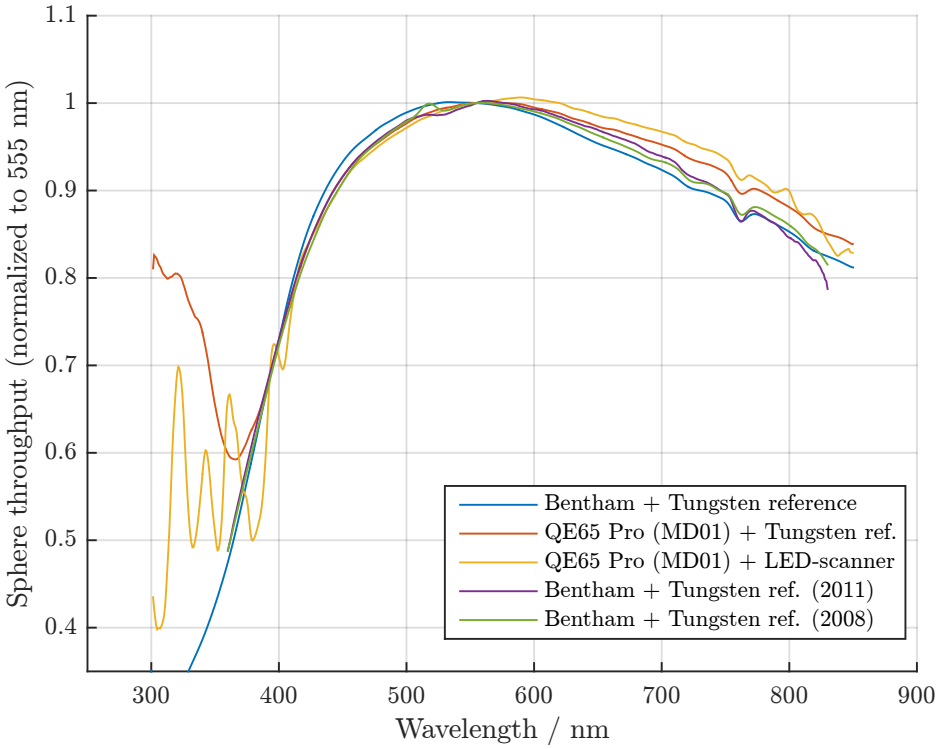

Figure 23: Sphere throughput measured with different methods, and throughput measurements from 2008 and 2011 as comparison.

The throughput calculated using the two different methods are shown in Figure 23. Also measurement results from 2008 and 2011, which were carried out using a scanning spectroradiometer and a tungsten reference lamp, are shown as a comparison.

It should be noted that the spectral throughput results from the measurements carried out with the QE65 Pro are consistent with each other, but differ significantly from the ones obtained with the Bentham DTMc300 at longer wavelengths. The difference of the measurements made with the QE65 Pro is in the same scale with the differences of the measurements made with a scanning spectroradiometer over the years. As the behavior of the Bentham DTMc300 spectroradiometer is studied more at the MRI than of the QE65 Pro, the throughtput obtained with it is used for the final results.

4.3 Illuminance uniformity of the external source

The illuminance distribution of the external lamp was measured on an optical rail. Two linear translators were assembled as XY-configuration for moving the HUT-1

photometer within the area corresponding to the 40-mm precision aperture used in the measurement of the reference luminous flux. The aperture is not used in this measurement. A sequence of ten different scans was performed. In each round the illuminance distribution of the lamp is scanned using the 5×5 grid shown in Figure 24.

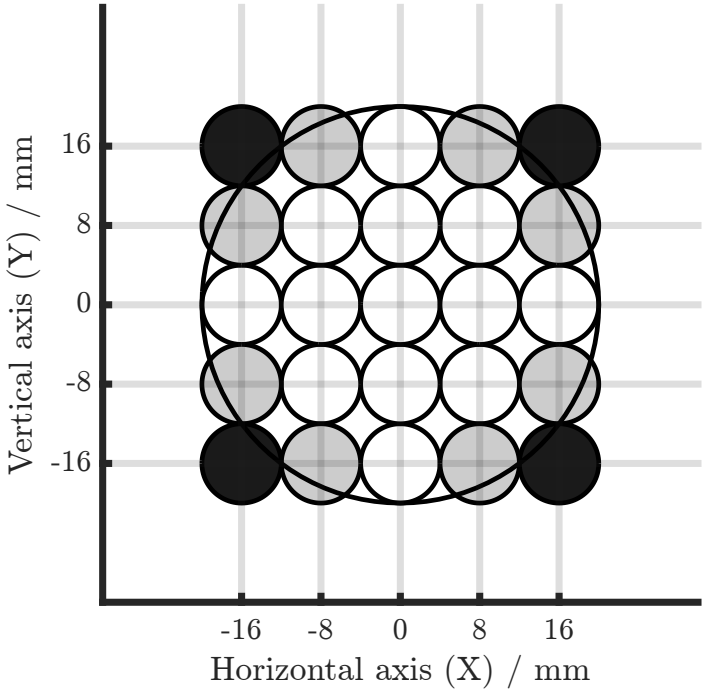

Figure 24: The measurement points for the illuminance uniformity of the external source.

The measurement points shown in grey are weighted with the area that lies inside the area of the precision aperture (the large circle in the figure). The weighting factor is calculated geometrically. The diameters of the precision aperture and the reference photometer aperture are 40 mm and 8 mm, respectively. Measurement points colored as black are discarded.

The correction factor is calculated for each scan as a weighted average of the values of measurement points on the grid relative to the center point. The resulting correction factor is an arithmetic mean of the coefficient of each round. Using the described method over 75 % of the area of the precision aperture is included in the calculation of the correction coefficient. The illuminance uniformity was calculated to be 0.9985 with standard deviation of 0.015 %.

5 Measurements of OLEDs

In this section the tested OLEDs and their measurements are introduced. Results acquired from goniospectrometer measurements are used for calculating the spatial non-uniformity corrections for each OLED. The integrating sphere based luminous flux measurements of OLEDs are detailed and the results are corrected with the combination of the calculated correction factors.

5.1 The studied OLED panels

The 6 tested OLEDs can be seen in Figure 25 and their specifications are listed in the Table 5. The specified correlated color temperatures for the panels were between 2800–3500 K. For Philips OLEDs CCT was not announced.

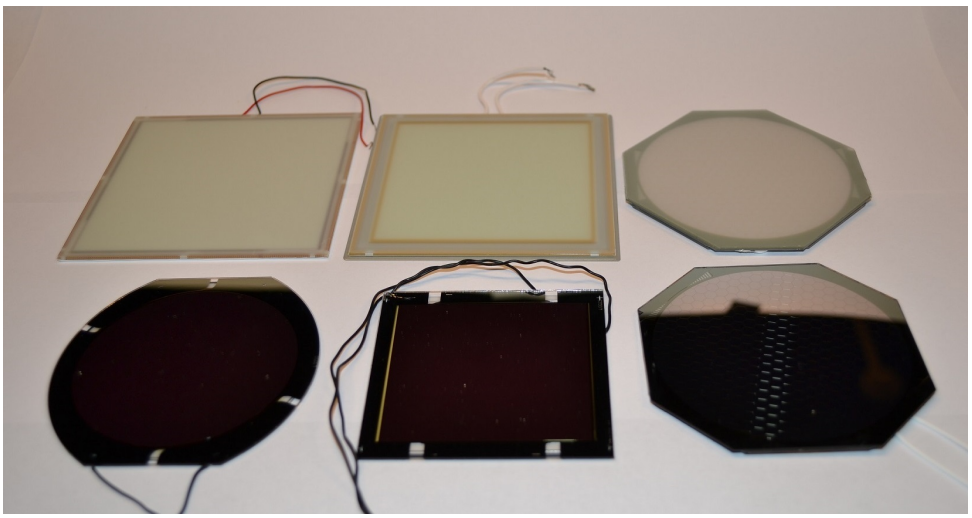

Figure 25: The tested 6 OLEDs clockwise starting from top-left corner in order: LG, Lumiotec, Osram 1, Osram 2, Philips 1, Philips 2.

Table 5: Specifications of the tested OLEDs.

OLED	Shape	Diffuse / Mirrored	Active area mm (x mm)	Supply current mA	Specified luminous flux
LG	Square	D	90 x 90	215	75
Lumiotec	Square	D	77.8 x 77.8	170	55
Osram 1	Round	D	79	186	-
Osram 2	Round	M	79	270	-
Philips 1	Square	M	61.4 x 60.53	0.2	-
Philips 2	Round	M	71	260	-

The Keithley SourceMeter 2420 is used to supply the current to the OLEDs and to monitor their voltage. The utilized current in the goniometric and integrating

sphere measurements for each panel was specified by the manufacturer as a rated or typical current. In case of only maximum value for current was specified, 75% of that value was used. The voltages of the OLEDs depend on the alignment and the ambient temperature. The electrical stability of the OLED and the ambient temperature were monitored during the measurement.

5.2 Measurements of the spectral and angular distributions

The relative angular distributions $I_{\mathrm{rel}}(\theta, \phi)$ of the tested OLEDs were measured in the goniospectrometer using Konica Minolta CS-2000A as a detector. The distance from the scanned OLED to the surface of the diffuser was set to 135 cm. The OLEDs were measured by rotating the panels around their center over two axes, the zenith angle going from -90° to 90° and the azimuth angle between 0° and 180°. For both of the rotation axes the step size was set to 5°. For viewing the differences in angular distribution for a diffuse and a mirrored surface OLEDs two panels (LG and Philips 1) from different manufacturers were chosen to a closer inspection. The angular distributions of all of the tested OLEDs using the discussed normalizations methods are shown in Appendix B.

In Figure 26 is shown the angular irradiance distribution of the spectrum for the LG and Philips 1 panels. The distributions are normalized to the maximum spectral value at zenith angle 0°. The LG panel has a descending irradiance at all wavelengths when the viewing angle is increased. The OLED by Philips has close to a constant illuminance up to the zenith angle of 25° at the wavelength of 609 nm (main peak). The peak with the wavelength of 455 nm has maximum value at the angle of 35°.

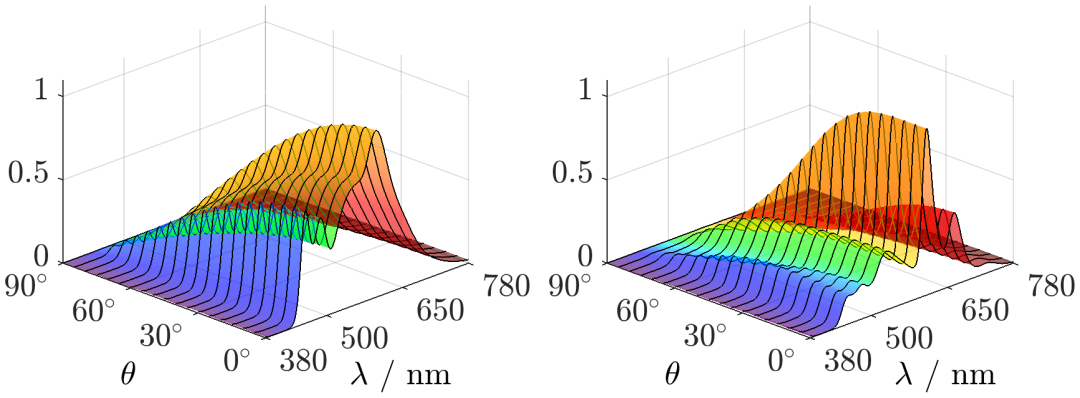

(a) LG

(b) Philips 1

Figure 26: The distribution of the spectral intensity of the diffuse LG and mirrored Philips 1 panels as a function of the zenith angle and normalized to the maximum value at the zenith angle of 0°.

When the irradiance is normalized to the value at the wavelength of 555 nm separately in each zenith angle, it is seen (Figure 27) that the spectral shape of the LG panel is independent of the viewing angle. Similar behavior was seen in all the

tested OLEDs with diffuse surface. In contrast, the peak at 529 nm of the Philips 1 panel compared to the irradiance level at 555 nm increases at larger viewing angles, whereas for the peaks at other wavelengths the normalized irradiance decreases.

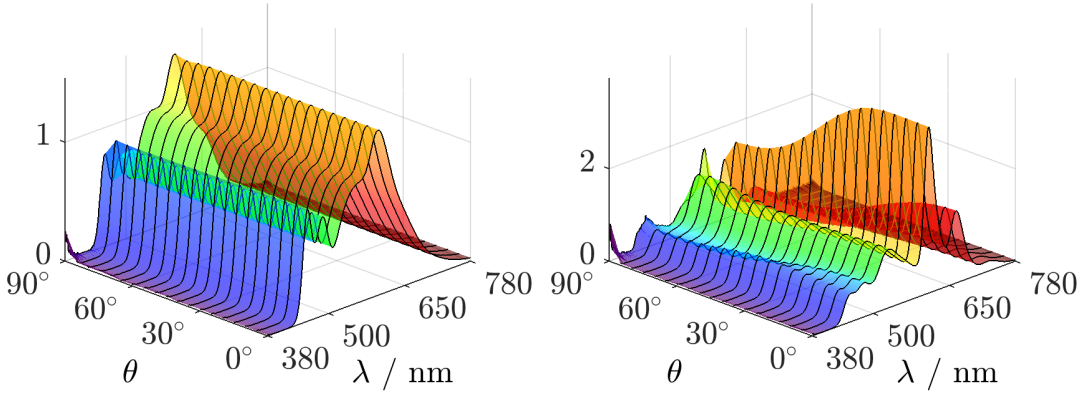

(a) LG (b) Philips 1

Figure 27: The distribution of the spectral intensity of the LG and Philips 1 panels as a function of the zenith angle and normalized to the value at wavelength of 555 nm in each zenith angle separately.

The LG panel has close to a Lambertian radiation pattern, as can be seen from Figure 28, where the irradiance is normalized to the cosine of the zenith angle. The normalized irradiance at 70° viewing angle is still 90 % of the value measured at the surface normal. Similar radiation pattern was observed for all of the diffuse surface OLEDs. On the other hand, the radiation pattern of the mirrored Philips 1 differs significantly from the radiation of a Lambertian emitter.

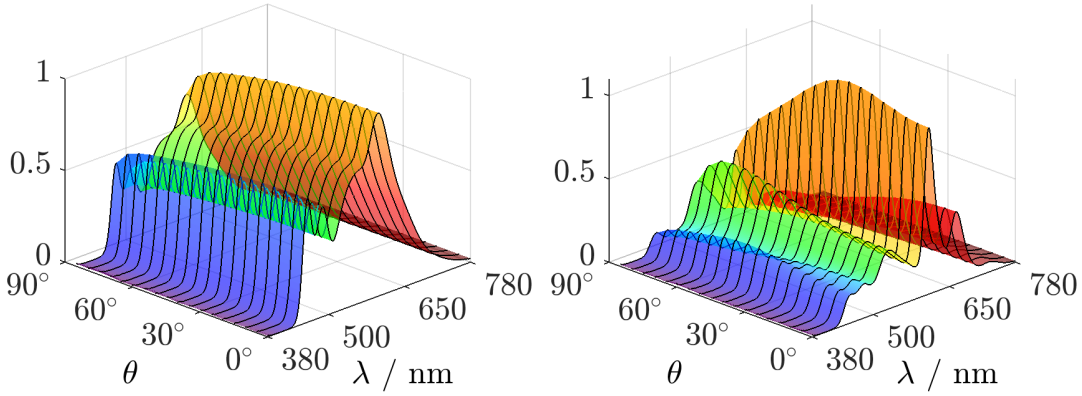

(a) LG (b) Philips 1

Figure 28: The distribution of the spectral intensity of the LG and Philips 1 panels normalized to the cosine of the zenith angle.

The edge emission of the Philips 1 panel was measured in the goniospectrometer using the same measurement distance and geometry as for the main surface emission.

The light radiating out of the main surface towards the measurement equipment was blocked with black absorbing material and all the edges were left unobstructed. The OLED was positioned vertically on the goniometer so that the center of one edge of the OLED lay on the point of rotation of the setup (Figure 7).

The OLED was rotated in 5° steps first about the center of the measured edge on a horizontal axis perpendicular to the optical axis and after that about the vertical axis shown in Figure 7. The result of this measurement is shown in Figure 29a. The measurement was repeated with one angle of ϕ (0°) and in the direction of θ from -55° to 55° with 0.5° resolution. The emission profile of the measurement is shown in Figure 29b.

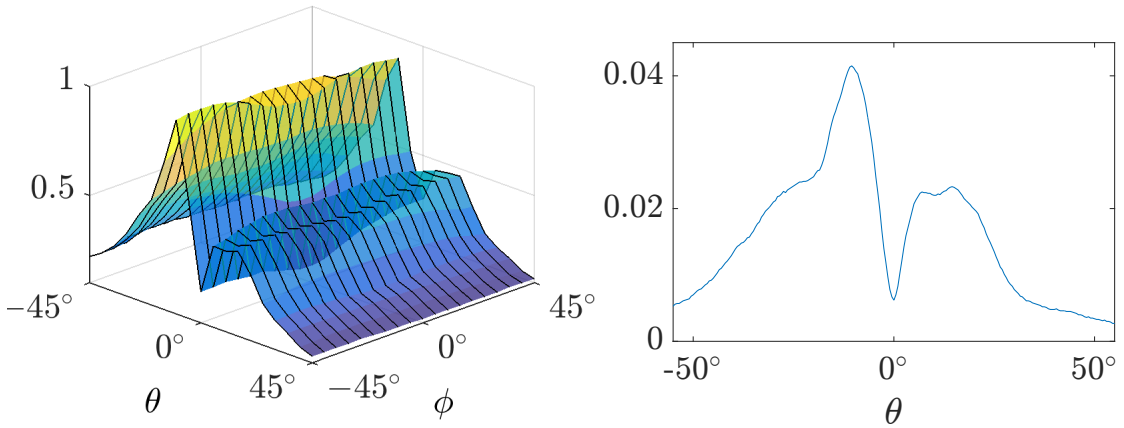

Figure 29: The edge emission of the tested Philips 1 OLED. Figure (a) shows the angular distribution about two axis in 5° steps. The graph is normalized to the maximum value. In (b) is the angular distribution measured about one axis in 0.5° steps.

The most intensive radiation angle was seen at 10° to the back-side of the OLED. The tested OLED does not have any significant change in the edge emission pattern as a function of ϕ. At the normal to the surface of the edge only small part of the maximum value of the edge emission was measured. This corresponds with the previous research made [10]. The total radiation of the edge can be approximated from the measurement results over one axis as an integral of the measured intensity in one direction multiplied by 2π. The integrated edge emission is 0.7 % of the total measured main surface emission.

5.3 Analysis of spatial non-uniformity corrections

For the calculation of the spatial correction for the internal source k_{int} at different orientations, the intensity distribution of the tested OLED was rotated to wanted direction on a virtual sphere. The intensity distribution is rotated by first transforming the spherical coordinate system to a Cartesian, multiplying the intensity distribution data with rotation matrices, using an interpolation to match the points of the

distribution to the ones of the SRDF map, and finally transforming back to the spherical coordinates. After this, the spatial correction for the OLED is calculated according to Equation 10.

The spatial correction was calculated for all of the tested OLEDs in three orientations ($\{0°, 0°\}$, $\{90°, 0°\}$ and $\{135°, 315°\}$) both photometrically and spectrally. The orientations correspond to the bottom of the sphere, the direction of the auxiliary port, and a point 45° toward the top of the sphere from the reference point, respectively.

To study the effect of misalignment of the OLED on the uncertainty of the spatial correction, a Monte Carlo simulation of 500 points was performed for all the OLEDs photometrically and spectrally. The orientation of the OLED was misaligned randomly relative to the original orientation. A rectangular distribution with maximum deviations of 5°, 10°, and 25° was used for both horizontal and vertical deflection angles (Figure 30). The uncertainty of the spatial correction is directly proportional to the maximum deflection angle. In the final uncertainty analysis, the maximum deflection angle of 10° is used.

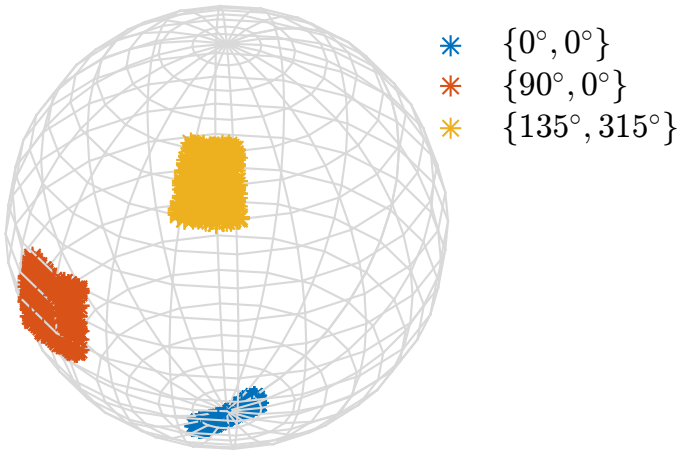

Figure 30: Orientation distribution for misalignment of the OLED in the integrating sphere for three different positions with ±10° of uncertainty angle.

5.3.1 Photometric spatial correction for the internal source

Figure 31 shows the spatial correction coefficients calculated from the normalized SRDF measured with the photometer for each OLED in three different positions with orientation uncertainty of 10°. The expanded uncertainty ($k = 2$) of k_{int} due to the misalignment is smallest at the direction towards the auxiliary port {90°, 0°} in the sphere. Near the points at the sphere bottom {0°, 0°} and 45° up from the reference point {135°, 315°}, the the uncertainty due to the misalignment is higher.

The absolute value for the spatial correction coefficient from the photometric measurements is 1.0080 ± 0.0015 with the level of confidence of 95 % for all the OLEDs in all three orientations. The spatial corrections of all the OLEDs with

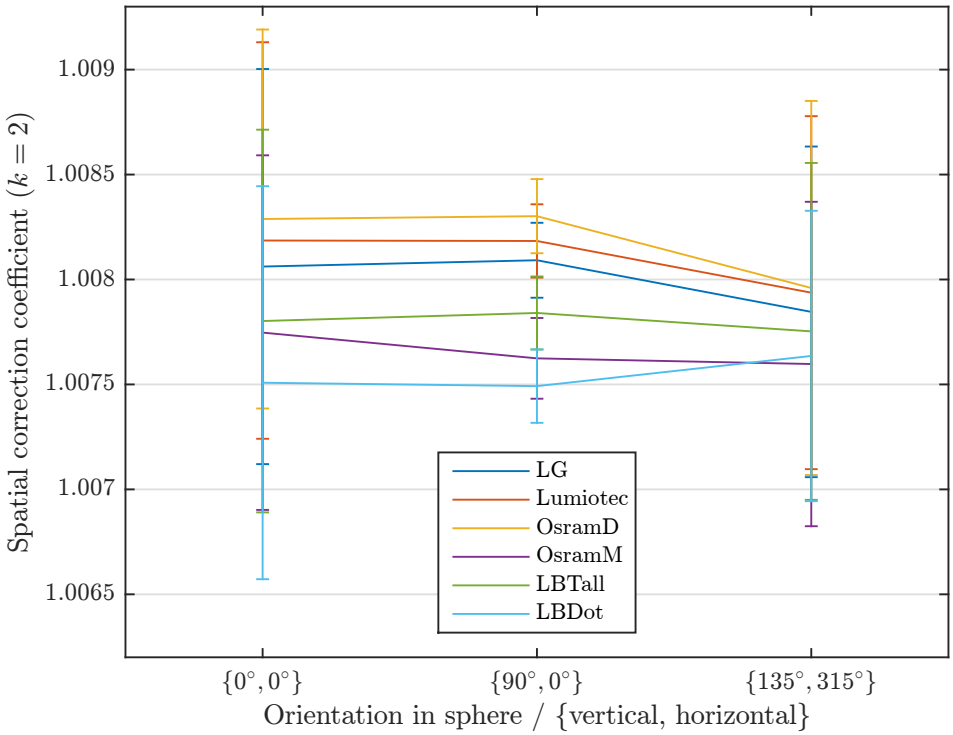

Figure 31: Photometric spatial correction coefficient measured using the photometer LM-1. The error bars correspond to the expanded uncertainty ($k = 2$) due to the misalignment of maximum 10° of the OLEDs in the sphere.

diffuse surfaces is higher than those with mirrored surfaces in all three orientations. This is consistent with the finding that the surface type has a significant effect on the angular distribution of the OLEDs, as was discussed in Section 5.2.

Based on these results, the spatial correction of OLEDs can be divided into two groups based on whether the emitting surface is diffuse or mirrored. The coefficients with photometrically measured SRDF of the integrating sphere of MRI for OLEDs with mirrored and diffuse surface are shown in Table 6.

Table 6: Photometric spatial correction coefficients for mirrored and diffuse surface OLED measured using the photometer LM-1.

Orientation	Mirrored	Diffuse
{0°, 0°}	1.0077 ± 0.0011	1.0082 ± 0.0011
{90°, 0°}	1.0077 ± 0.0004	1.0082 ± 0.0003
{135°, 315°}	1.0077 ± 0.0009	1.0079 ± 0.0009

The photometric spatial correction coefficients calculated from the SRDF measured with spectroradiometer QE65 Pro are shown in Figure 32. The photometric values were calculated using Equation 2. For the orientations towards the points {0°, 0°} and {90°, 0°} on the sphere the correction coefficient calculated with the SRDF measured with the spectroradiometer are 1.0075 ± 0.0010 with 95 % confidence

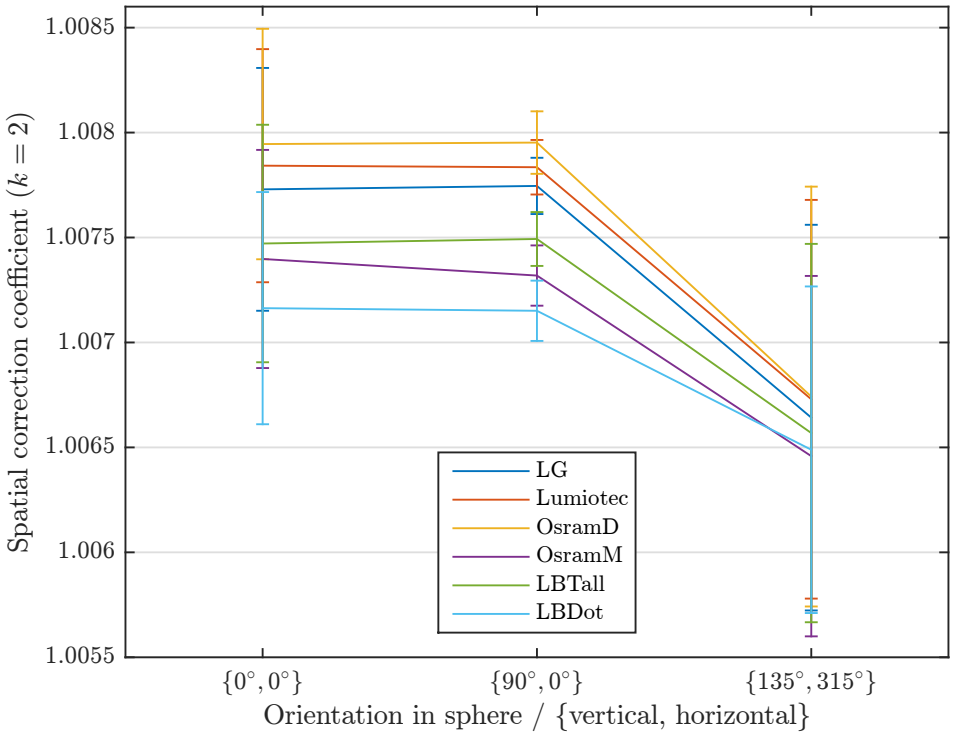

Figure 32: Photometric spatial correction coefficient measured using the diffuser head MD01 and spectroradiometer. The error bars correspond to the expanded uncertainty ($k = 2$) due to the misalignment of maximum 10° of the OLEDs in the sphere.

level. For the point {135°, 315°} the correction coefficient is 1.0067 ± 0.0012.

The coefficients are close to the ones measured with LM-1 except at the point $\{135°, 315°\}$ where the results are almost 0.15 % lower compared to the other two points. Some of the inconsistency may be explained with the poor f_2 value of the diffuser head of the spectroradiometer, but the exact reason for this behavior needs to be further studied. Similar effect of the surface type of an OLED on the spatial correction coefficient is seen in the case of SRDF measured with spectroradiometer as was discovered in the case of measurements made with the photometer.

5.3.2 Spectral spatial correction for the internal source

In Figure 33 are shown the spatial correction coefficients as a function of wavelength for all of the tested OLEDs facing towards the bottom of the integrating sphere. For the two other analyzed directions the graphs are shown in Appendix C.

The spatial correction of the OLEDs with diffuse surface decreases rather linearly with wavelength at the wavelength range of 500–750 nm. Whereas the panels with mirrored surface have significant oscillation as a function of wavelength. It should be noted that the coefficient of the panels with diffuse surface has similar wavelength dependency than the k_{comp} calculated for the virtual Lambertian emitter in Figure 21.

When comparing the spectral coefficients with the ones measured with the pho-

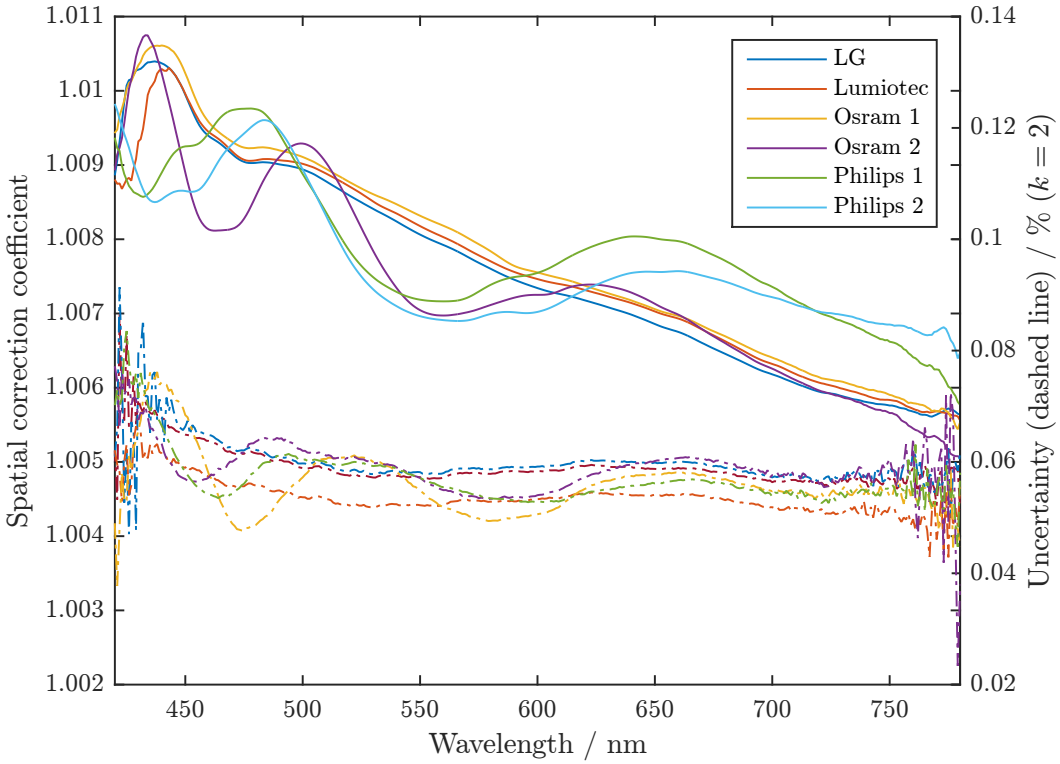

Figure 33: The spectral spatial correction and the relative expanded uncertainty ($k = 2$) due to misalignment of maximum 10° of the OLEDs (dashed line) for all the tested panels facing towards the bottom of the sphere.

tometer, there is no significant difference seen in the uncertainties due to misalignment. The variation in the spectral coefficients at each wavelength is smaller when the panel is facing to point {135°, 315°} on the sphere. Similar behavior was seen in the photometric coefficients.

5.4 Measurements with the integrating sphere

Measurements of OLEDs in the integrating sphere were performed in three orientations, facing towards bottom of the sphere (shown in Figure 34), auxiliary port and a point 45° to top of the sphere from the reference point, for inspecting the possible effect of the orientation of the OLED on the luminous flux. In every position the OLED was allowed to stabilize for 10–15 minutes and after this a measurement sequence of 10 points with an integration time of 0.2 seconds was performed for 30 times with the photometer LM-1. The photometric measurement sequence took approximately two minutes for all of the tested OLEDs.

After the photometric measurement the detector was changed for the spectroradiometer QE65 Pro with the MD01 diffuser head. Another set of 30 measurements was performed with integration times between 16 and 60 seconds depending on the luminous flux output of the OLED. For panels with the lowest luminous flux output, a set of 60 measurements was used for achieving lower SNR instead of

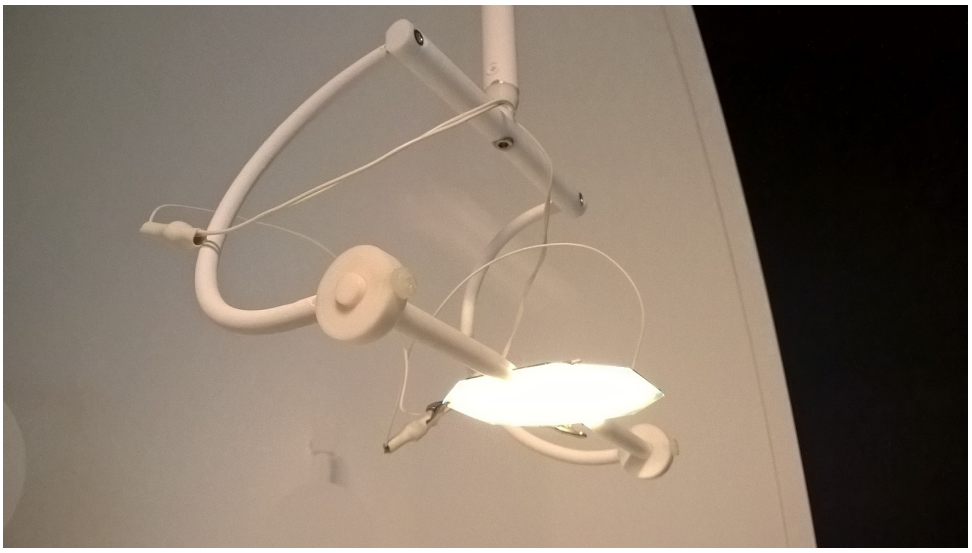

Figure 34: OLED attached to the OLED holder [18] and pointing towards the bottom of the sphere in the integrating sphere measurements.

30 measurements. The duration of the spectral measurement sequence varied from 10 minutes up to an hour depending on the panel. The integrated spectrum of the tested OLEDs, measured in the integrating sphere and corrected with the measured spectral correction factors are shown in Figure 35. For the spectral spatial correction, correction at the sphere bottom was used.

The self-absorption coefficient was measured for each OLED separately. Only the position where the tested OLEDs face towards the bottom of the sphere was used. In Figure 36 are shown the spectral self-absorption correction coefficients from the measurements. OLEDs manufactured by Osram and Philips absorb light at wavelength of 400 nm significantly more compared to the rest of the measured wavelength range. It should be noted, that whether the emitting surface of the OLED is mirrored or diffuse does not define the spectral shape of the self-absorption for the 6 tested OLEDs. The photometric self-absorption coefficients for the Lumiotec panel was 1.048 and for rest of the panels α was between 1.030 and 1.037.

The measured color corrections for the tested OLEDs (c_i) and for the external source (c_e) are shown in the Table 7. The methods (1), (2) and (3) correspond to the throughput measurements made with the Bentham DTMc300 with tungsten reference lamp, the QE65 Pro with tungsten reference lamp and the new method based on the sphere scanner, respectively. Based on the results, the color correction coefficient does not depend on the orientation of the OLED in the sphere and thus the average of the coefficients in different orientations is given in the table. The way the throughput is measured has a noticeable impact on the color corrections. The values calculated from the measurements made with the method (1) are used in the final analysis as was mentioned in Section 4.2.

The measured photocurrents from the measurements of the OLEDs in the integrating sphere and the calculated values of luminous flux are presented in Table 8 as an average for all of the tested orientations in the sphere. The luminous flux is

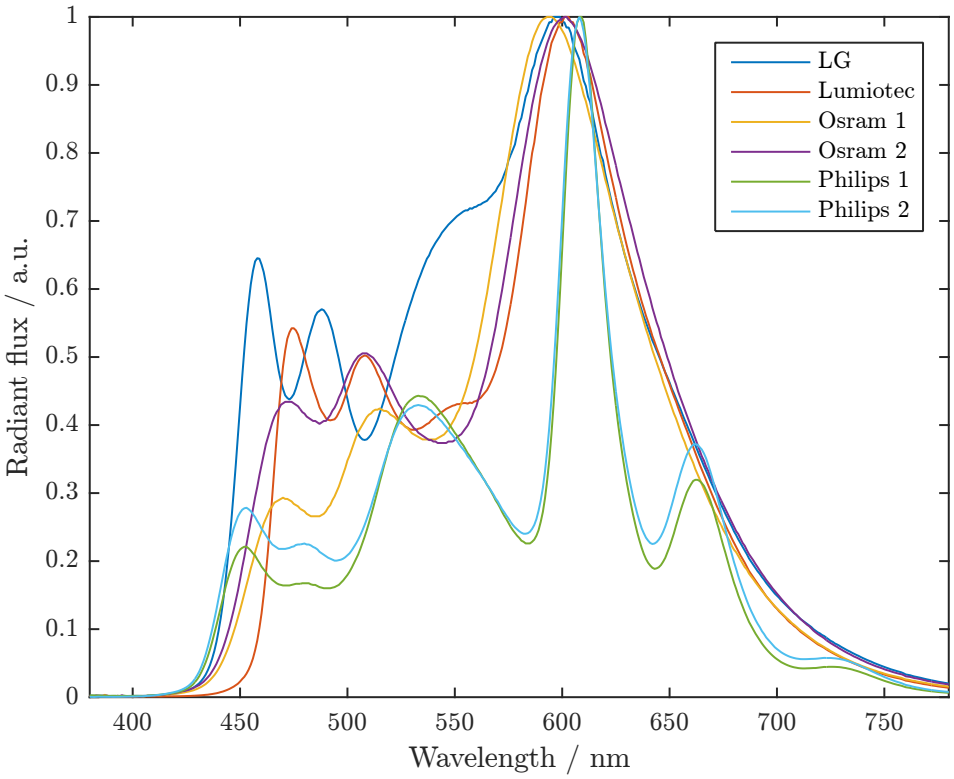

Figure 35: The spectral radiant flux of the tested OLEDs, normalized to the maximum value of the spectrum.

Table 7: Calculated color correction coefficients for the tested OLEDs and for the external source with different spectral throughput measurement methods.

	(1)	(2)	(3)
External source	1.00013	1.00002	1.00001
LG	0.99914	1.00108	1.00563
Lumiotec	1.00100	1.00290	1.00744
Osram 1	1.00138	1.00332	1.00788
Osram 2	1.00154	1.00345	1.00799
Philips 1	1.00154	1.00346	1.00800
Philips 2	1.00156	1.00348	1.00802

obtained by measuring the external source with calibrated photometer according to Equations 5 and 6. The results are corrected with the discussed correction coefficients. The standard deviation is calculated from the luminous flux at different orientations. For the LG and Lumiotec panels the measured luminous flux is within 5 % of the value specified value by the manufacturer.

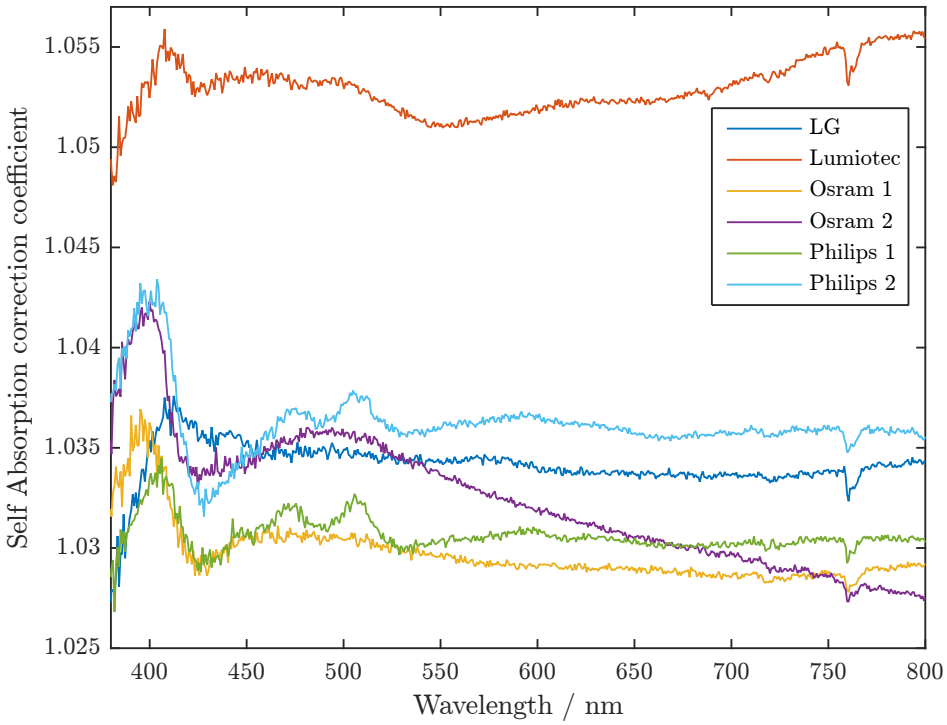

Figure 36: The self-absorption correction coefficients $\alpha(\lambda)$ for the tested OLEDs.

Table 8: Measured photocurrents and luminous flux of the OLEDs in the integrating sphere as an average of the different orientations, and the standard deviation of the luminous flux of different orientations.

	Photocurrent	Luminous flux	Standard deviation	Electrical power	Standard deviation
LG	579 nA	71.68 lm	0.19 %	1.33 W	0.10 %
Lumiotec	443 nA	54.86 lm	0.21 %	1.37 W	0.09 %
Osram 1	112 nA	13.91 lm	0.52 %	0.65 W	0.32 %
Osram 2	92.3 nA	11.43 lm	0.63 %	0.95 W	0.20 %
Philips 1	195 nA	24.08 lm	0.35 %	1.47 W	0.34 %
Philips 2	224 nA	27.73 lm	0.15 %	1.92 W	0.37 %

5.5 Uncertainty analysis of OLED luminous flux

The uncertainty analysis of the luminous flux measurement of a typical and a problematic OLED is presented in Table 9.

The uncertainty of the luminous flux responsivity of 0.3 % covers the components caused by the production of the external reference flux and the calibration of the sphere responsivity. When the sphere responsivity is calibrated once for the empty sphere, and the actual lamp measurements are performed on the following days, the effect of the drift of the sphere photometer to the uncertainty is 0.1 %. [4]

The stability of the luminous flux of OLED was obtained by opening and closing the integrating sphere and monitoring the stabilization of the OLED. The change of

Table 9: Simplified uncertainty budget of luminous flux measurement of OLED.

	100 × relative uncertainty	
Source of uncertainty	Typical OLED	Problematic OLED
Luminous flux responsivity	0.3	0.3
Drift of the sphere photometer	0.1	0.1
Stability of the luminous flux	0.05	0.2
Photocurrent measurement	< 0.01	< 0.01
Spectral mismatch correction, $c_\mathrm{i}/c_\mathrm{e}$	0.2	0.2
Self-absorption correction, α	0.2	0.2
Spatial non-uniformity correction		
for internal source, k_int	0.06	0.06
for external source, k_ext	0.06	0.06
Combined standard uncertainty	0.44	0.48
Expanded uncertainty ($k = 2$)	0.88	0.96

the temperature inside the sphere produced for a problematic OLED an uncertainty of 0.2 % in the stabilized photocurrents over several measurements. For a typical OLED the standard deviation was 0.05 %.

The uncertainty of the photocurrent measurement ($< 0.01\%$) takes into account the standard deviation of the photocurrents in OLED measurement, as well as the uncertainties associated with current-to-voltage converter and the digital multimeter.

The uncertainty related to the spectral mismatch correction is dominated by the uncertainty in the relative spectral responsivity of the photometer. The effect of the wavelength accuracy on the spectral measurement of the OLED by shifting the spectrum of the OLEDs by 1 nm towards shorter and longer wavelengths was tested. An uncertainty of 0.02 % was calculated based on the tests using rectangular distribution. As the uncertainty of wavelength accuracy in the OLED spectrum was not significant, the total uncertainty of the spectral mismatch correction is estimated as 0.2 % based on the previous research [4].

The uncertainty of the self-absorption correction of 0.2% was obtained by calculating the relative standard deviation of the repeated measurements of the empty sphere during the photometric self-absorption correction measurements. The geometrical differences of the measurement with the auxiliary lamp compared to the external source is taken into account in the uncertainty.

The uncertainty of the spatial non-uniformity correction for an OLED inside the sphere was calculated from the uncertainty due to the misalignment in the sphere towards the bottom of the sphere and was based on the Monte Carlo simulation. For a direction {90°, 0°} in the sphere the uncertainty is 0.03 % as was shown in Figure 31.

The uncertainty due to the spatial correction of the external source is approximated from the difference of the k_ext values of the spatial non-uniformity scans made with LM-1 and QE65 Pro using rectangular distribution.

6 Conclusions

In this work methods for measuring luminous flux and spectral radiant flux of OLEDs using an integrating sphere were developed. The integrating sphere setup at the MRI was optimized for OLED measurements and thoroughly characterized.

To improve the usable range of the spatial uniformity scan of the integrating sphere, the sphere scanner was modified by changing a new warm white LED with over two times higher irradiance level at wavelengths over 600 nm compared to the original cold white LED. In addition, a new diffuser for the spectroradiometer measurements was developed with over 60 % increase in the transmittance compared to the existing Bentham D7 type diffuser.

With the enhancements of the measurement setup, the spatial responsivity of the integrating sphere could be characterized photometrically with over 14 % better SNR. The spatial uniformiy of the integrating sphere was also characterized spectrally. It was found out that the spectral SRDF map changes as a function of the wavelength. The spatial correction calculated for a virtual Lambertian source had 0.4 % linear decrease from wavelength 450 nm to 730 nm.

A new method, based on the spatial non-uniformity scanning of the integrating sphere spectrally, for calculating the spectral throughput of the integrating sphere was introduced. The throughput of the sphere obtained with the QE65 Pro was 0.3 % larger at 700 nm than the throughput measured with Bentham DTMc300. In addition, a new analyzing method of the illuminance uniformity of the external source in the integrating sphere method was introduced. The new measurement sequence covers 75 % of the area of the precision aperture over the previous 52 %.

The angular properties of OLEDs were studied and it was found out that the panels with diffuse surface have emission pattern close to a Lambertian emitter, whereas OLEDs with mirrored surface had up to 35° viewing angle quite constant emission. The surface type of the OLED caused 0.05 % difference to the spatial correction coefficient. The edge emission of one OLED was measured to be 0.7 % of the main surface emission of the panel.

The spatial corrections of the OLEDs facing towards different positions in the integrating sphere were studied both photometrically and spectrally. The uncertainty due to a misalignment of the OLED in the sphere was found out to depend on the direction the OLED is aligned to in the sphere. For the bottom of the sphere the uncertainty was 0.06 %, whereas pointing towards the auxiliary port the uncertainty is 0.03 %. Based on the measurements the uncertainty is not affected by the surface type of the panel. The difference of the photometric spatial correction coefficient measured with a photometer and a spectroradiometer was 0.5 %.

Luminous flux measurements with OLED in the integrating sphere were performed. It was found out that the OLEDs' operating positions caused at maximum 0.6 % difference in the luminous flux. This suggests that in accurate measurements the measurement position should match the final usage position. The expanded uncertainty ($k = 2$) for measuring a typical OLED was 0.88 %.

References

[1] "Publishable JRP Summary Report for Project ENG05 Lighting: Metrology for Solid State Lighting." http://www.m4ssl.npl.co.uk/wp-content/uploads/2012/12/Publishable-JRP-Summary-ENG05-SSL-2012-11-25.pdf. Accessed 15.11.2015.

[2] "Publishable JRP Summary Report for ENG62 MESaIL: Metrology for Efficient and Safe Innovative Lighting." http://www.euramet.org/Media/docs/EMRP/JRP/JRP_Summaries_2013/Energy_JRPs/ENG62_Publishable_JRP_Summary.pdf. Accessed 15.11.2015.

[3] "Aalto Energy Efficiency Research Programme." http://aef.aalto.fi. Accessed 15.11.2015.

[4] T. Poikonen, T. Pulli, A. Vaskuri, H. Baumgartner, P. Kärhä, and E. Ikonen, "Luminous efficacy measurement of solid-state lamps," *Metrologia*, vol. 49, no. 2, p. S135, 2012.

[5] T. Kawabata and Y. Ohno, "Optical measurements of OLED panels for lighting applications," *Journal of Modern Optics*, vol. 60, no. 14, pp. 1176–1186, 2013.

[6] L. Pereira, *Organic Light-Emitting Diodes: The Use of Rare-Earth and Transition Metals*. Pan Stanford Publishing Pte. Ltd., 2012.

[7] M. Klein, K. Heuser, F. Schindler, B. Krummacher, T. Dobbertin, R. Pätzold, and C. Gärditz, "OLED lighting: light where it never has been before," in *Integrated Optoelectronic Devices 2007*, pp. 64860E–64860E–10, International Society for Optics and Photonics, 2007.

[8] B. Lüssem, M. Furno, and K. Leo, "Highly efficient pin-type OLEDs," in *Organic light-emitting diodes (OLEDs): Materials, devices and applications* (A. Buckley, ed.), Woodhead Publishing Ltd., 2013.

[9] K. Saxena, D. S. Mehta, R. Srivastava, and M. Kamalasanan, "Surface and edge emission in organic light emitting devices," *Optics communications*, vol. 267, no. 2, pp. 416–421, 2006.

[10] J.-S. Kim, P. K. Ho, N. C. Greenham, and R. H. Friend, "Electroluminescence emission pattern of organic light-emitting diodes: Implications for device efficiency calculations," *Journal of Applied Physics*, vol. 88, no. 2, pp. 1073–1081, 2000.

[11] B. D'Andrade, "Phophorescent OLEDs for solid-state lighting," in *Organic light-emitting diodes (OLEDs): Materials, devices and applications* (A. Buckley, ed.), Woodhead Publishing Ltd., 2013.

[12] "The basis of physical photometry," *CIE 18.2-1983*.

[13] M. S. Rea, *Lighting handbook: reference & application.* Illuminating Engineering Society of North America, 1993.

[14] J. Hovila, "Valovirran kansallisen mittanormaalin käyttöönotto ja testaus (in finnish)," Master's thesis, Teknillinen Korkeakoulu, 2001.

[15] W. L. Wolfe, *Introduction to radiometry*, vol. 29. SPIE Press, 1998.

[16] M. L. Rastello, E. Miraldi, and P. Pisoni, "Luminous-flux measurements by an absolute integrating sphere," *Applied optics*, vol. 35, no. 22, pp. 4385–4391, 1996.

[17] Labsphere Inc., "Technical guide: Reflectance materials and coatings." `https://www.labsphere.com/wp-content/uploads/2015/02/a-guide-to-reflectance-materials-and-coatings.pdf`. Accessed 15.10.2015.

[18] M. Santaholma, T. Poikonen, J. Askola, T. Pulli, and E. Ikonen, "Luminous efficacy measurement of OLEDs using an integrating sphere," in *Proceedings of NEWRAD 2014*, 2014.

[19] Y. Ohno, "Integrating sphere simulation: application to total flux scale realization," *Applied optics*, vol. 33, no. 13, pp. 2637–2647, 1994.

[20] S. Winter, M. Lindemann, W. Jordan, U. Binder, and M. Anokhin, "Convenient integrating sphere scanner for accurate luminous flux measurements," *Metrologia*, vol. 46, no. 4, p. S248, 2009.

[21] Y. Ohno, M. Lindemann, and G. Sauter, "Analysis of integrating sphere errors for lamps having different angular intensity distributions," *Journal of the Illuminating Engineering Society*, vol. 26, no. 2, pp. 107–114, 1997.

[22] "Colorimetry - part 2: CIE standard illuminants," *ISO 11664-2:2007(E)/CIE S 014-2*, 2006.

[23] Konica Minolta Inc., "Spectroradiometer CS-2000/CS-2000A: Instruction manual." `http://www.konicaminolta.com/instruments/download/instruction_manual/display/pdf/cs-2000-2000a_instruction_eng.pdf`. Accessed 25.10.2015.

[24] Ocean Optics, "QE65 Pro data sheet." `http://oceanoptics.com/wp-content/uploads/OEM-Data-Sheet-QE65Pro.pdf`. Accessed 23.10.2015.

[25] Bentham Instruments Ltd, "DTMc300: Double monochromator." `http://www.bentham.co.uk/pdf/DTMc300.pdf`. Accessed 20.10.2015.

[26] T. Pulli, P. Kärhä, and E. Ikonen, "A method for optimizing the cosine response of solar UV diffusers," *Journal of Geophysical Research: Atmospheres*, vol. 118, no. 14, pp. 7897–7904, 2013.

[27] "Methods of characterizing illuminance meters and luminance meters," *CIE Publ. No 69 (Vienna: International Commission on Illumination)*, 1987.

[28] T. Poikonen, P. Blattner, P. Kärhä, and E. Ikonen, "Uncertainty analysis of photometer directional response index f_2 using Monte Carlo simulation," *Metrologia*, vol. 49, no. 6, p. 727, 2012.

A Drawings of the MD01 diffuser head

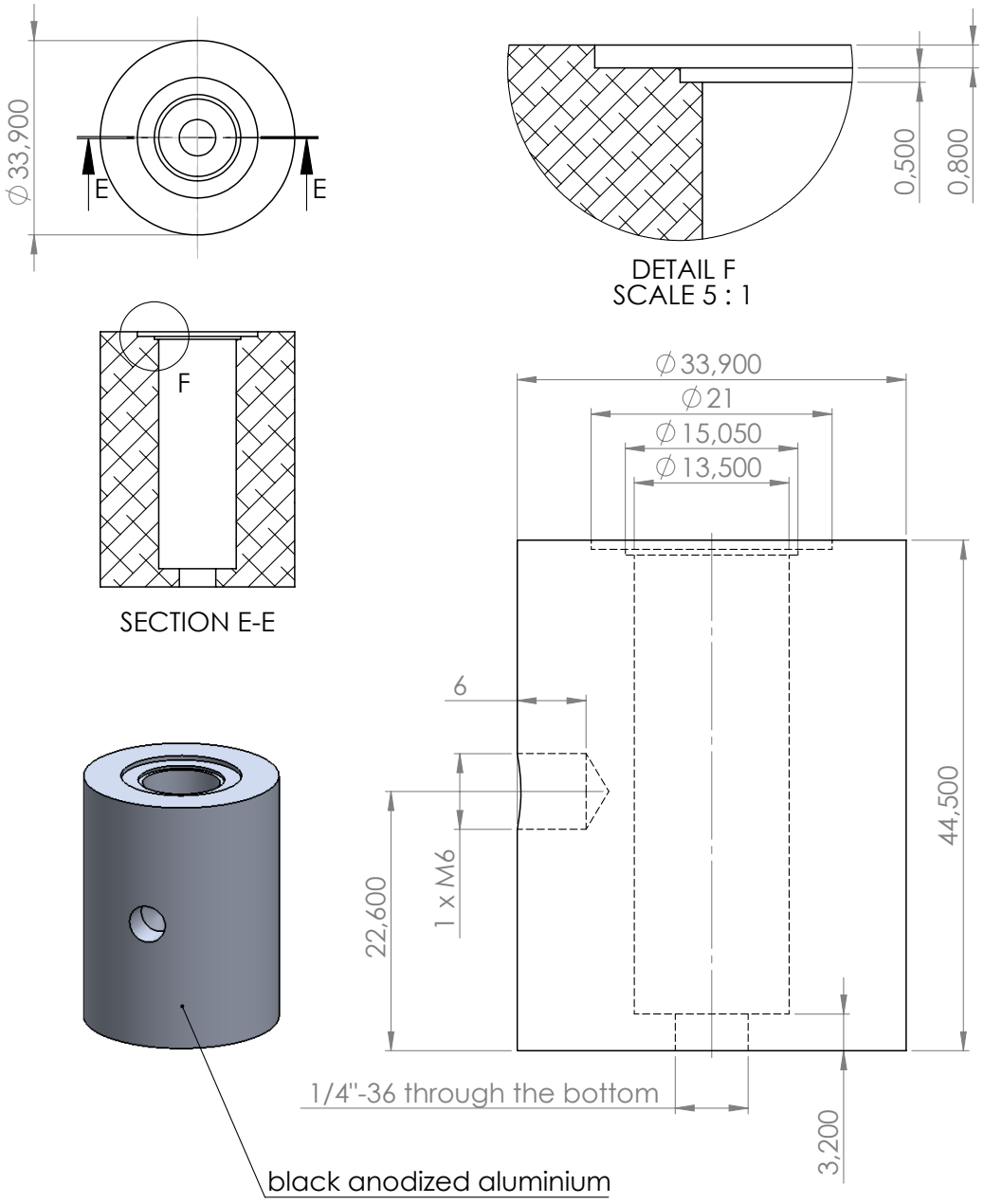

B Spectral and angular distributions of the tested OLEDs

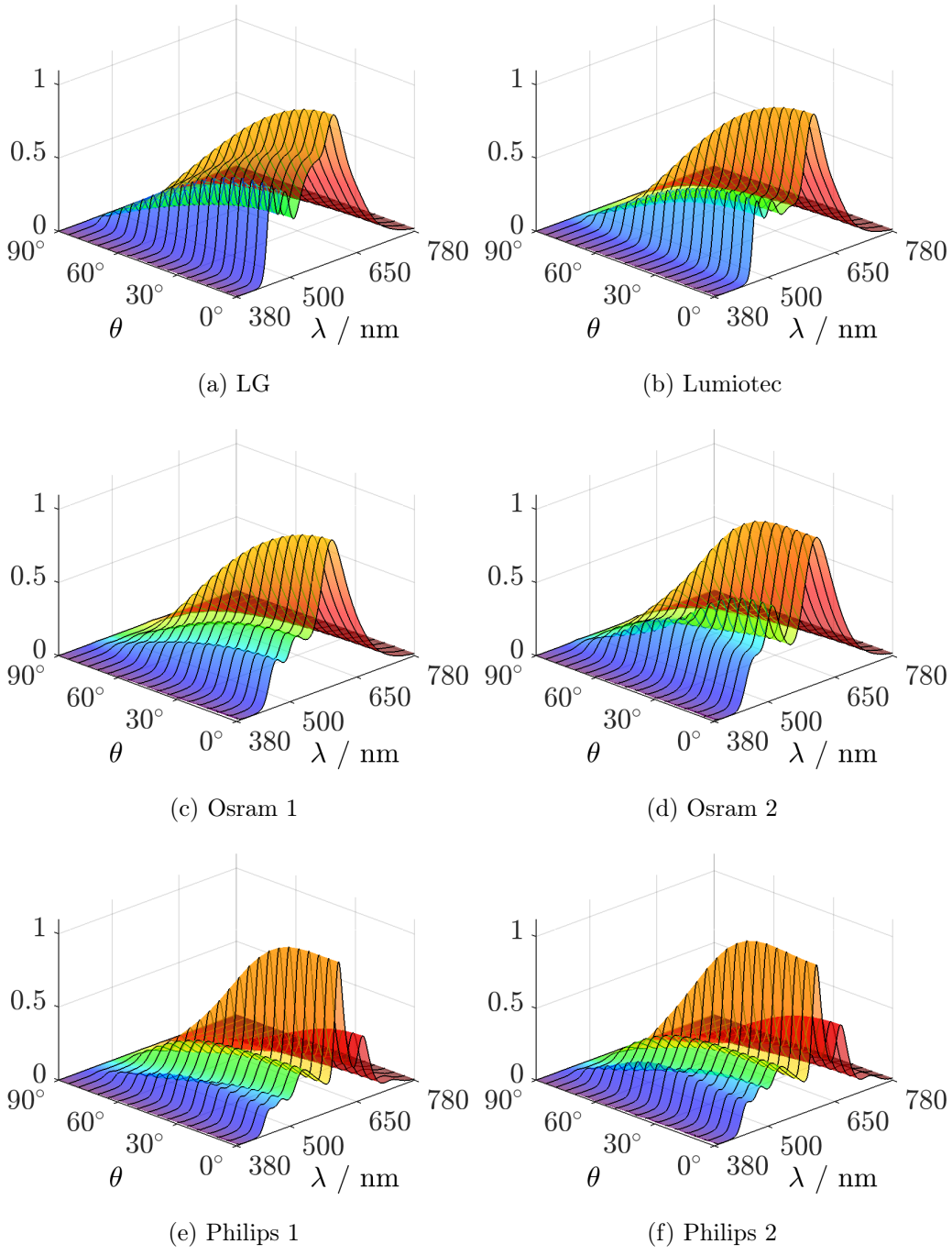

(a) LG

(b) Lumiotec

(c) Osram 1

(d) Osram 2

(e) Philips 1

(f) Philips 2

Figure B1: The distribution of the spectral intensivity of the tested OLEDs as a function of the zenith angle and normalized to maximum value at zenith angle 0°.

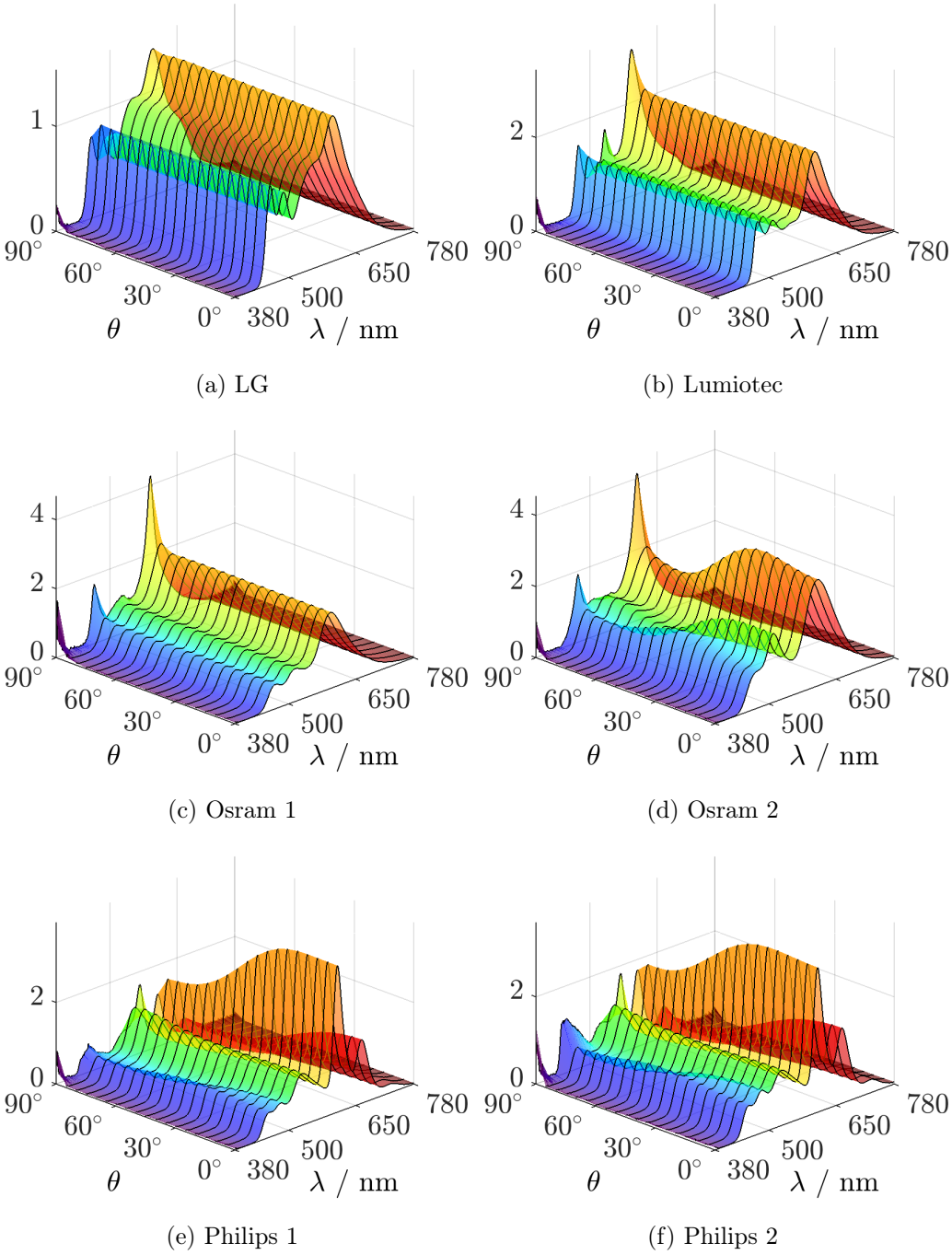

(a) LG

(b) Lumiotec

(c) Osram 1

(d) Osram 2

(e) Philips 1

(f) Philips 2

Figure B2: The distribution of the spectral intensivity of the tested OLEDs as a function of the zenith angle and normalized to the irradiance at 555 nm at all angles.

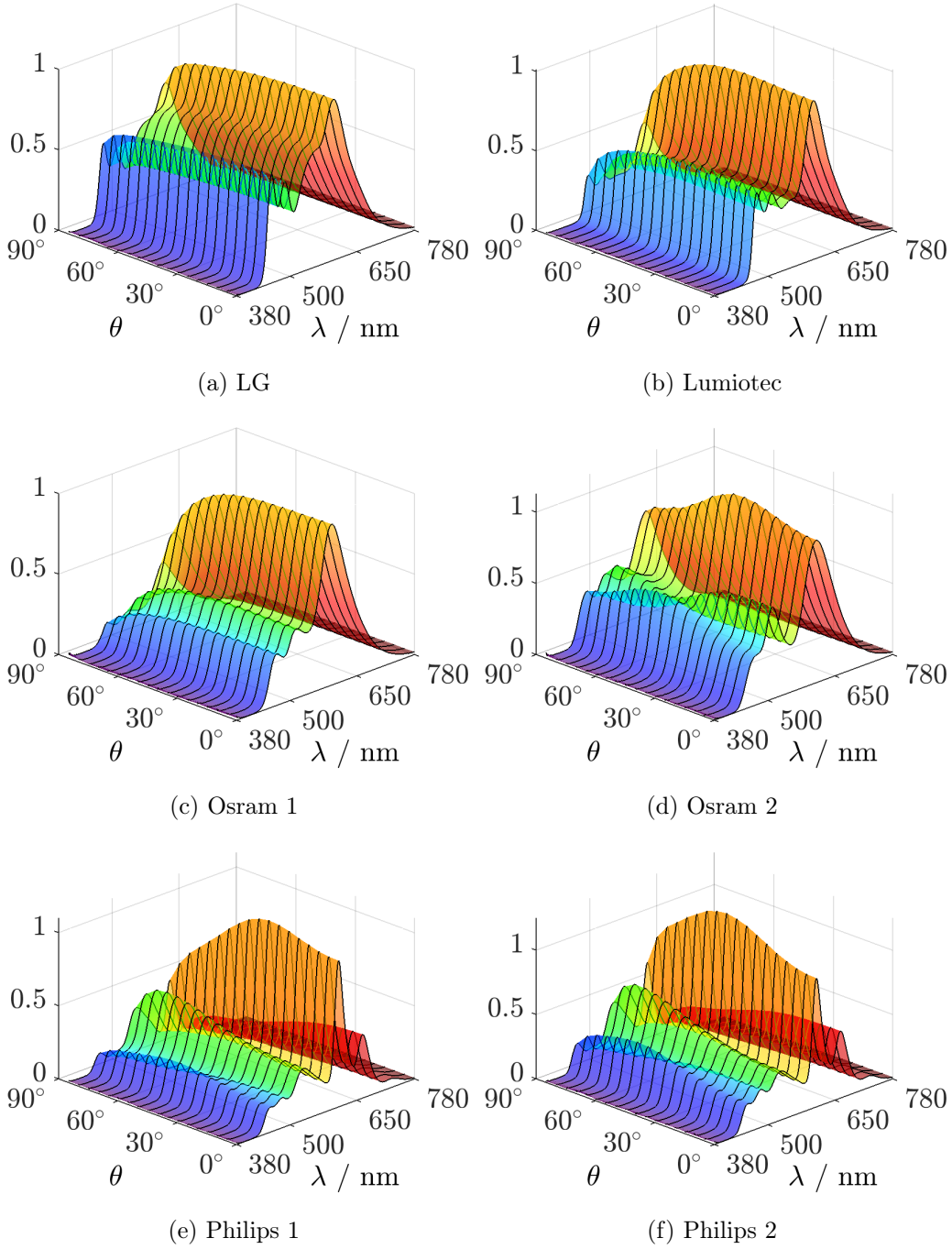

(a) LG

(b) Lumiotec

(c) Osram 1

(d) Osram 2

(e) Philips 1

(f) Philips 2

Figure B3: The distribution of the spectral intensivity of the tested OLEDs normalized to the cosine of the zenith angle

C Spectral spatial correction for internal source on two orientations in the sphere

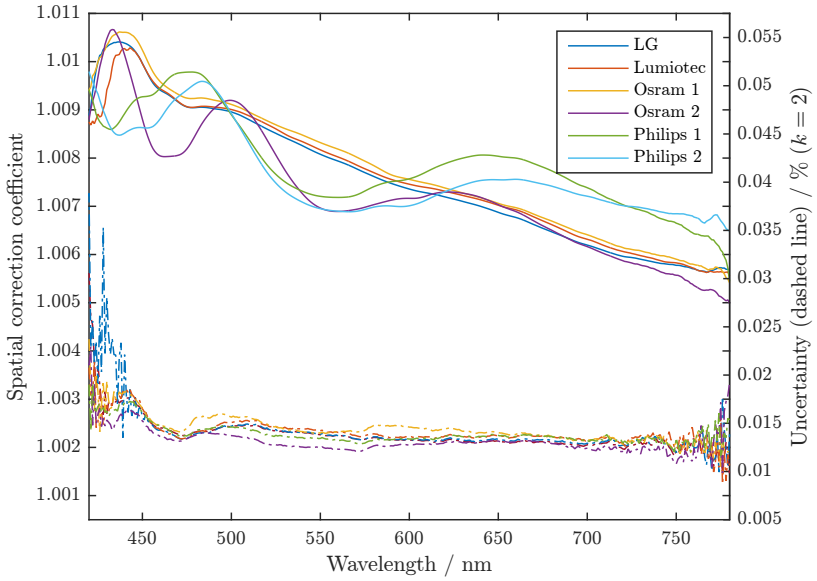

Figure C1: The spectral spatial correction and the orientation uncertainty (dashed line) of 10° for all the tested OLEDs facing towards the auxiliary port in the sphere.

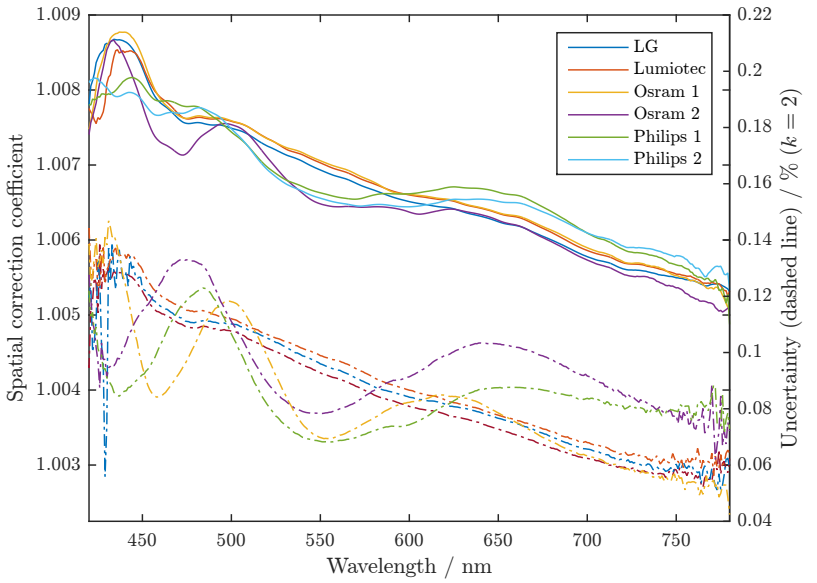

Figure C2: The spectral spatial correction and the orientation uncertainty (dashed line) of 10° for all the tested OLEDs facing the point {135°, 315°} on the sphere surface.